Prediction of common-mode currents on cables connected to a multilayer printed circuit board and couplings on the board

tu/e
Research Report
ISSN 0167-9708
Coden: TEUEDE

Eindhoven
University of Technology
Netherlands

Faculty of Electrical Engineering

Prediction of Common-Mode Currents on Cables Connected to a Multilayer Printed Circuit Board and Couplings on the Board

by
F.B.M. van Horck
A.P.J. van Deursen

EUT Report 97-E-305
ISBN 90-6144-305-9
August 1997

Eindhoven University of Technology Research Reports

EINDHOVEN UNIVERSITY OF TECHNOLOGY

Faculty of Electrical Engineering
Eindhoven, The Netherlands

ISSN 0167-9708 Coden: TEUEDE

PREDICTION OF COMMON-MODE CURRENTS ON CABLES CONNECTED TO A MULTILAYER PRINTED CIRCUIT BOARD AND COUPLINGS ON THE BOARD

by

F.B.M. van Horck
A.P.J. van Deursen

EUT Report 97-E-305
ISBN 90-6144-305-9

Eindhoven
August 1997

CIP-DATA LIBRARY TECHNISCHE UNIVERSITEIT EINDHOVEN

Horck, F.B.M. van

Prediction of common-mode currents on cables connected to a multilayer printed circuit board and couplings on the board / by F.B.M. van Horck and A.P.J. van Deursen.
- Eindhoven : Eindhoven University of Technology, 1997. - (Eindhoven University of Technology research reports ; 97-E-305).
ISBN 90-6144-305-9
NUGI 832
Trefw.: elektromagnetische interferentie / gedrukte bedrading / elektromagnetische koppelingen.
Subject headings: electromagnetic compatibility / printed circuits / crosstalk.

Prediction of Common-Mode Currents on Cables Connected to a Multilayer Printed Circuit Board and Couplings on the Board

F.B.M. van Horck and A.P.J. van Deursen

Abstract

Common-mode (CM) currents generated by circuits on a triple layer printed circuit board with a continuous ground plane have been studied by means of a transmission-line (TL) model. The CM current flows through the shields of attached cables; the CM emission from these cables often dominates the direct radiation of the board. Several boards with different complexity were studied in the frequency domain. For demonstration purposes a digital board with modern digital electronic was developed. Measurements between 100 kHz – 1 GHz confirm the TL models. The crosstalk on the boards was also studied up to 1 GHz. Return tracks and grounding planes with interruptions were discussed as an example for other grounding structures. A first step for the implementation of the TL model into the design stage of a product was studied.

Keywords: electromagnetic compatibility, EMC, electromagnetic interference, EMI, common-mode currents, multilayer boards, crosstalk, transfer impedance, printed circuit board, PCB, printed wiring board, PWB, layout printed circuit.

Horck, F.B.M. van and A.P.J. van Deursen
Prediction of common-mode currents on cables connected to a multilayer printed circuit board and couplings on the board.
Eindhoven: Faculty of Electrical Engineering, Eindhoven University of Technology, 1997.
EUT Report 97-E-305, ISBN 90-6144-305-9

Address of the authors:
High Voltage and EMC Group
Faculty of Electrical Engineering
Eindhoven University of Technology
P.O. Box 513, 5600 MB Eindhoven, The Netherlands

E-mail: f.b.m.v.horck@ele.tue.nl
a.p.j.v.deursen@ele.tue.nl

Acknowledgement

This research is supported by the Dutch Technology Foundation (STW) in project number ETN11.2508. The skillful technical assistance by ing. Peter R. Bruins is gratefully acknowledged. The authors also appreciate the stimulating discussions with dr. Jos R. Bergervoet from Philips Research Laboratories, and prof. Piet C.T. van der Laan of our group. The authors also thank the students J.A. Kaland, P.C.J.M. van der Wielen, and H.J. Zwier for their experimental contributions during the practical work or final exam work.

Contents

Prediction of Common-Mode Currents on Cables Connected to a Multilayer Printed Circuit Board and Couplings on the Board

I. Introduction

The radiation properties of wire structures were studied extensively since Hertz' discovery in 1886 of the wireless electromagnetic system. From these studies, see e.g. [1, 2, 3], it is known that single wire structures (antennas) radiate much more efficiently than two wire structures within their vicinity, such is the case for transmission-lines (TLs).

Translated to a printed circuit board (PCB): the tracks linking the components form many TLs or, in EMC terminology, differential-mode (DM) circuits. In the last decade the DM emission from PCB structures was calculated [4 — 8]. Cables are intended to transport the DM signals from and to a PCB. But the cables are also a part of the common-mode (CM) circuit, and act as efficient antenna's because of their length. The CM emission by the cables often dominates the DM emission from the PCB's. This has been predicted by Ott [9] and verified afterwards by several other people, see e.g. [10 — 19].

In modern EMC immunity and emission pre-compliance tests, CM currents through cables are injected or measured. This CM current based method was introduced by Bersier [20] to replace the extensive standard tests in which electromagnetic (EM) fields are applied or measured at larger distance from the equipment. Nowadays pre-compliance tests even largely suffice to demonstrate conformity with the European EMC requirements.

Bergervoet's *et al.* [21] CM skeleton model bears resemblance to Bersier tests. In that model the PCB and all components are modelled by CM voltage-sources at edges of the PCB, which drive the CM current into each cable attached to the PCB. Bergervoet *et al.* determined the sources and their internal impedances by measurements. Alternatively, a program as Fasterix [22] may calculate the sources: an equivalent network of the PCB and its components substitutes a full EM wave analysis. Even for simple PCB's the calculation still takes many hours, a long time in the design stage of a product.

The aim of this study is also to predict the CM currents which flow over the cables attached to the PCB, from the known the DM currents on the PCB. The tracks and the CM circuit are modelled as a set of coupled transmission lines. In combination with accurate analytical approximations to be presented for the TL parameters, the TL approach strongly reduces the computational effort or the hardware requirements. The comparison of the results with actual measurements was encouraging. A modern personal computer calculates different configurations in a few minutes; track positioning, placement of decoupling capacitors etc. could be optimized in a short time.

In the previous report [23] which we will call Report I, we described the coupling between a PCB and it's environment (CM circuit) through the transfer impedance. Figure 1 shows the structure studied. The coupling between the tracks and the CM circuit is described by a

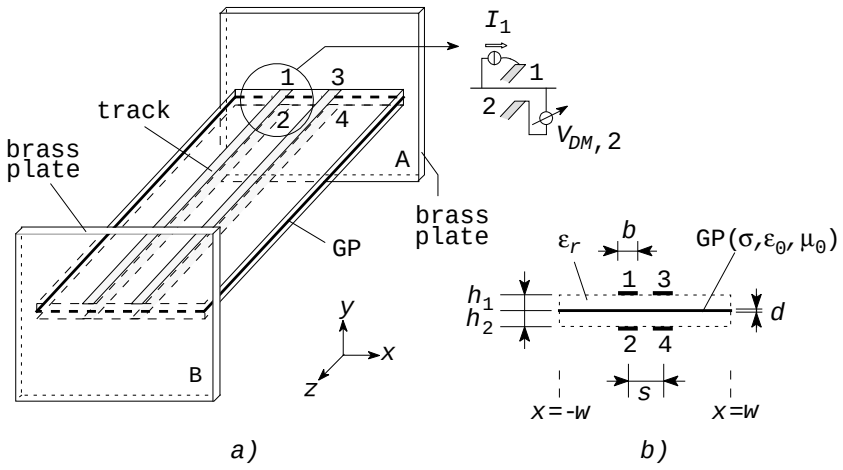

Fig. 1. Four tracks on a triple layer PCB which is mounted between two brass plates A and B. The tracks of width b and the ground plane (GP) are shorted to plate B. The current I_1 injected in track 1 on top returns through the ground plane (middle layer). For the DM-DM coupling we measure the voltage between track 2 (lowest layer) and the ground plane at the sending end. b) cross-section of the PCB.

transfer impedance Z_t per unit length [23, Eq. (1)]

$$Z_t = \frac{V_{DM,2}}{I_1 \ell}. \tag{1}$$

Our earlier two-dimensional (2D) model focussed on the magnetic coupling. The setup had finite length ℓ of 20 cm; resonances showed up in the measurement of Z_t [23, Figs. 18, 19, and 21] up to 1 GHz. To describe the resonances properly we should consider the finite length and we should include the capacitive coupling or transfer admittance Y_t. However, in a setup (Fig. 2) similar to the one proposed by Bersier [20], a total transfer impedance Z_T can be defined

$$Z_T = \frac{V_{CM}}{I_1}, \tag{2}$$

which relates a DM current (I_1) injected in track 1 to the equivalent voltage-source (V_{CM}) at the edge of the PCB. For setup of Fig. 2 the common-mode current I_{CM} then equals $V_{CM}/(Z_{CM} + 150)$. Throughout this report we adopt the total transfer impedance concept (with capital T as subscript) for both the DM-CM coupling and the DM-DM crosstalk; in the definition of the latter we then remove ℓ from Eq. (1).

The 150 Ω resistor in Fig. 2b models the CM-radiation resistance of a cable at resonance. A good EMC criterion for emission is the 3 μA 'rule of thumb' limit (see [23, Sect. VIII] and [24, Sect. 2.4.1]). If an actual cable is attached to the PCB, the CM-current distribution can be calculated by an integral equation method. From this CM-current distribution through the cable the far field can be established, see e.g. Ramo [25, Chapter 12] and Balanis [26].

The reciprocal situation, the immunity problem, can also be handled by the Bersier method. When an electromagnetic wave illuminates the cable (see [27] and references therein), a CM voltage-source at the edge of the PCB may be chosen to replace the cable and the wave. A CM current through the ground plane of the PCB then induces disturbing voltages in the DM circuits. Again, direct coupling between wave and DM circuits is often less important.

The experimental triple layer PCBs were 20 cm long. The copper GP had a conductivity $\sigma = 5.8 \cdot 10^7 (\Omega\text{m})^{-1}$ and a thickness $d = 30$ μm. The $b = 1.5$ mm wide tracks were placed at

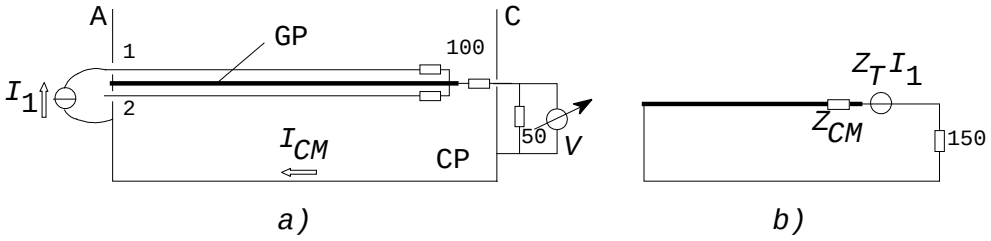

Fig. 2. a) Setup for pre-compliance measurements with current injection through track 1. The CM current is measured via the 150 Ω load. b) The PCB is replaced by a voltage source $Z_T(\omega)I_1$; the CM impedance Z_{CM} is formed by the ground plane (GP) of the PCB and by the cabinet panel (CP).

$h_{1,2} = 1.5$ mm above and below the GP (see Fig. 1). The epoxy layer on both sides of the GP had a dielectric constant ε_r of 4.7. Details of the measurements are given in Sect. VII of Report I.

Report I dealt with the DM-DM crosstalk and DM-CM coupling for straight tracks (Fig. 1), starting from the frequency dependence of the lateral current distribution in the ground plane. At the resonance frequencies the current distribution is essentially frequency independent. In this report we assume such a high-frequency (HF) distribution.

In EMC practice the common-mode current is most important and any model should focus on it. From this point of view the DM to CM crosstalk would be discussed first, and then the DM-DM coupling. Nevertheless, we reverse the order in this report. We hope this demonstrates more clearly the effects involved, for instance in case of the common-mode current generation without nearby metallic cabinet plane.

Section II describes the TL model of the DM-DM coupling for the simple straight tracks (Fig. 1). We focus on the coupling between tracks on opposite sides, because this situation is theoretically and experimentally more challenging. In Section III we discuss the TL model for Bersier setup as a straightforward extension of the DM-DM model. Printed circuit boards with more complicated tracks, i.e. tracks with several bends, are discussed in Sect. IV. Our TL model and the design rules from Report I can be implemented into software for PCB design; a flow chart is given in Sect. V. For demonstration purposes we developed two boards with HCT and HLL digital logic. The DM-CM coupling of these boards is treated in Sect. VI. Finally, Sect. VII deals with some lesser quality grounding structures which are encountered in practical PCBs: grounding traces rather than planes, or planes with interruptions perpendicular to the signal traces.

II. High-frequency effects of the simple DM structure

a. Transmission-line description

The dominant mode in a microstrip line is quasi-TEM: a TEM wave adapted to include a nonhomogeneous dielectric by modifying the line capacitance, and the conductor losses by adding a series resistance. Gupta *et al.* [28] give an overview of the vast literature published over the last decades.

Figure 3 shows our four tracks as coupled microstrip lines TL1-TL4 with the ground plane (GP) as reference; $z = 0$ corresponds with the side of plate A (near end) and $z = \ell$ with the

side of plate B (far end). The TL5 describes the CM current through the GP; its return is a second panel, for instance a cabinet panel (CP in Report I), or free space. In Sect. IV of Report I we saw that a second order coupling (DM-CM-DM) becomes important for small values of Z_t between tracks, as was suggested to us by Bergervoet [29]; we then had to include TL5. In this report the DM-CM-DM coupling can be neglected, i.e. TL5 absent, until in Sect. II.e where we discuss small Z_t's again.

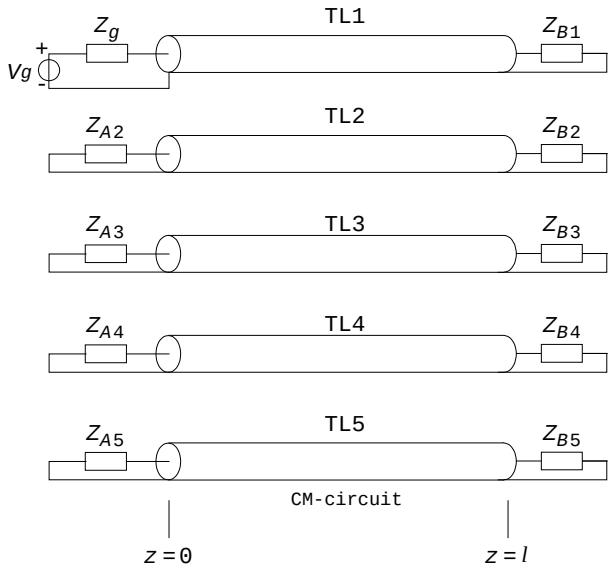

Fig. 3. Transmission-line (TL1-TL4) model of the four track PCB in Fig. 1; TL5 incorporates the DM-CM couplings as discussed in the main text. The near side $z = 0$ corresponds with the side of brass plate A, the far end $z = \ell$ with brass plate B. The terminating impedances are discussed in the main text.

The voltage source V_g with impedance Z_g injects a current in circuit 1. The other impedances depend on the actual situation studied, for instance, $Z_{Bi} = 0$, $i = 1, \cdots, 4$ for the shorted situation at brass plate B (Fig. 1.); see also sections II.d and II.e. The response of the system can be calculated from the impedance matrix $\mathbf{Z}(\omega)$ and admittance matrix $\mathbf{Y}(\omega)$ per unit length. Djordjević *et al.* [30] presented an overview of the methods to solve the coupled lines for linear and non-linear load impedances, both in frequency and time domain. We will first consider linear loads in the frequency domain; this allows us to employ the modal expansion of Djodjević and Sarkar [31]. Later on digital MOS circuits are discussed (Sect. VI). The input impedance of a MOS device is slightly nonlinear, whereas the output impedance is more nonlinear. Both impedances are linearized, therefore the modal expansion is applicable for such circuits.

b. TL parameters

Let us first consider a single track of width b at a height h on a dielectric above a GP of infinite extent.

Characteristic impedance

The characteristic impedance $Z_m = \sqrt{L_s/C_s}$ of this microstrip line is given e.g. by Gupta *et al.* [28]; L_s and C_s are the self inductance and self capacitance of the track w.r.t. the GP.

For convenience we repeat here Gupta's expressions (Eq. (2.116))

$$Z_m = \begin{cases} \frac{\eta}{2\pi\sqrt{\varepsilon_{r,eff}}} \ln\left(\frac{8h}{b} + 0.25\frac{b}{h}\right) & , \quad \frac{b}{h} \leq 1, \\ \frac{\eta}{\sqrt{\varepsilon_{r,eff}}} \left\{\frac{b}{h} + 1.393 + 0.667 \ln\left(\frac{b}{h} + 1.444\right)\right\}^{-1} & , \quad \frac{b}{h} > 1, \end{cases} \tag{3}$$

and

$$\varepsilon_{r,eff} = \frac{\varepsilon_r + 1}{2} + \frac{\varepsilon_r - 1}{2} \begin{cases} (1 + 12h/b)^{-1/2} + 0.04(1 - b/h)^2 & , \quad \frac{b}{h} \leq 1, \\ (1 + 12h/b)^{-1/2} & , \quad \frac{b}{h} > 1, \end{cases} \tag{4}$$

where $\eta = 120\pi\ \Omega$. The characteristic impedance Z_m and the effective dielectric constant $\varepsilon_{r,eff}$ depend on ε_r and b/h. The finite size of GP and dielectric increases Z_m; the deviation is less than 3 percent when the track is farther than $2b$ from the edge, as was shown by Smith and Chang [32].

The self-inductance L_s can be obtained from $L_s = Z_{0m}/c_0$, with Z_{0m} the characteristic impedance of the microstrip with the dielectric replaced by vacuum or $\varepsilon_{r,eff} = 1$, and c_0 the velocity of light in vacuo. For all tracks on our PCBs we use the same $L_s = 414$ nH/m, calculated as if the GP were of infinite extent. The capacitance $C_s = 88.9$ pF/m may be calculated from L_s and Z_m with the proper value of $\varepsilon_{r,eff}$ for the dielectric.

Series impedance

The series impedance Z_s for the track is

$$Z_s(\omega) = R_{DC} + R_s(\omega) + j\omega L_s, \tag{5}$$

where R_{DC} and $R_s(\omega)$ are the d.c. and skin-effect resistances. Closed-form expressions for the skin-effect resistance were first published by Pucel *et al.* [33] in 1968, where they used Wheeler's incremental inductance rule. Recently Collin obtained expressions by means of conformal mapping [34, Appendix III]. These values are somewhat higher than Pucel's one; Collin claims that his solution is in better agreement with experimental results [34, pp. 156-7]. For a microstrip structure with finite width GP (as in our case), Djordjević [35] gives also expressions for $R_s(\omega)$. The high frequency current distribution in a microstrip line and a rectangular strip is given in several papers by Faraji-Dana and Chow [36, 37, 38].

Coupled tracks, off-diagonal elements.

We now include the other tracks. The impedance matrix $\mathbf{Z}(\omega)$ per unit length for our problem (Figs. 1 and 2) is then given by

$$\mathbf{Z}(\omega) = Z_s(\omega)\mathbf{I}_4 + \mathbf{Z_t}(\omega), \tag{6}$$

in which $\mathbf{I}_4$ is a 4×4 identity matrix and $\mathbf{Z_t}(\omega)$ the transfer impedance matrix with zeros on the diagonal as described in Report I. For high frequencies, Report I also contains numerical and analytical approximations (based on conformal mapping) for the off-diagonal terms of the self-inductance matrix $\mathbf{L}$.

The admittance matrix $\mathbf{Y}(\omega)$ per unit length equals

$$\mathbf{Y}(\omega) = j\omega\mathbf{C}, \tag{7}$$

where $\mathbf{C}$ is the 4×4 capacitance matrix (see e.g. Van Bladel [39, Sect. 4.6]). It is more difficult to calculate the off-diagonal elements of the capacitance matrix because the boundary conditions on the dielectric. Appendix A presents an analytical foundation of the numerical treatment for static fields; the implementation adapts the discretization for highest accuracy. From these calculations we derived analytical approximations which suffice in our TL model and considerably speed up the computations for a PCB.

For convenience, suppose that only tracks 1 and 2 (Fig. 1) are present. The capacitance matrix then becomes

$$\mathbf{C} = \begin{bmatrix} C_s + C_{12} & -C_{12} \\ -C_{12} & C_s + C_{12} \end{bmatrix}. \tag{8}$$

In vacuo the capacitance matrix $\mathbf{C_0}$ satisfies the relation

$$\mathbf{L}\mathbf{C_0} = \frac{1}{c_0^2}\mathbf{I_2} \tag{9}$$

with

$$\mathbf{L} = \begin{bmatrix} L_s & M \\ M & L_s \end{bmatrix}, \tag{10}$$

the inductance matrix. We found the following approximate relation between C_{12} and $C_{12,0}$, the capacitive coupling coefficients with and without dielectric:

$$C_{12} \approx \frac{C_{12,0}}{\sqrt{\varepsilon_{r,eff}}}, \tag{11}$$

valid for $h_1 = h_2 = h$ and $b_1 = b_2 = b$. This simple relation agrees with the accurate numerical values to within 20 percent for tracks on the same or on different sides of the GP over a wide range of parameters: $1 \leq \varepsilon_r \leq 12$, $0.8 \leq b/h \leq 4$, and 50 mm $\leq 2w \leq$ 400 mm. See Appendix A4 for an example of the numerical and approximated C_{12} (of the order fF/m). The numerical diagonal elements of $\mathbf{C}$ were of course also in good agreement those given by Gupta's expressions (3) and (4).

c. Influence of CM and DM radiation on TL parameters

In Sect. IV of Report I we showed the importance of the differential to common-mode (DM-CM) conversion. Both the CM and DM current loops radiate energy. One may question the effect of radiation on the TL parameters, or on the attenuation and the distortion of the waves along the line.

This question has been answered long ago for wire antenna structures. For a PCB without cables attached to it, the GP replaces the thin wire as radiating element. Abraham [1] showed in 1901 for a single isolated half-wave dipole antenna, that the effect of the radiation is at first instance negligible compared to the 'Joulian losses' (i.e. skin-effect losses). Carson [2] and Manneback [3] arrived at the same conclusion when studying the effect of radiation from two wire transmission lines or traveling-wave antennas. The CM and DM currents were assumed to vary sinusoidally as function of position; see the recent paper by Tijhuis *et al.* [40]. We calculated the radiated power from the DM and the CM circuit with this current distribution; see Appendix B. Transmission line 1 (Fig. 3) or track 1 in Fig. 1a is energized and shorted at side B, i.e. $Z_{B1} = 0$. The source impedance Z_g equals the characteristic impedance Z_0 of TL1 and the voltage V_g is chosen such that a the amplitude I_1 of the DM current is 1 A.

Figure 4 shows the results as function of frequency for a 5 cm wide and $\ell = 0.2$ m long PCB; the other parameters used were $h_1 = 1.5$ mm and $\varepsilon_r = 1$ or 4.7. For comparison Collin's skin-effect loss is also incorporated.

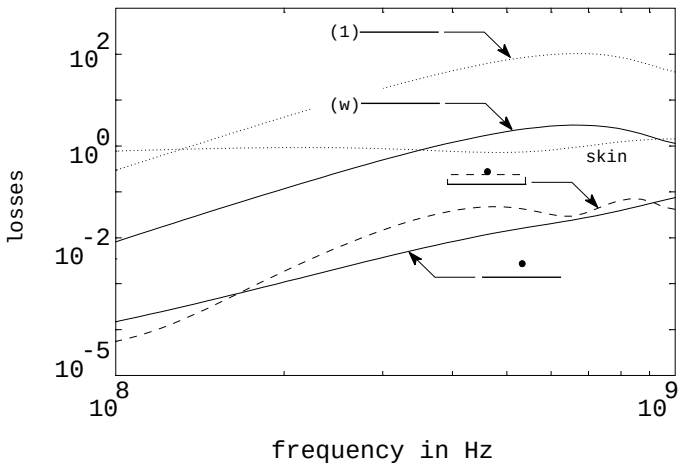

Fig. 4. Losses in Watts for a $2w = 5$ cm wide and $\ell = 20$ cm long PCB structure of figure 1; track 1 is energized with amplitude $I_1 = 1$ A. The DM-radiation loss is shown without dielectric (—) and with a dielectric layer (- - -) of $\varepsilon_r = 4.7$. The curve labeled 'w' shows CM-radiation loss with the worst case amplitude I_{CM} (see main text). For comparison, the curve labeled (1) shows the CM-radiation loss for $I_{CM} = 1$ A; the one labels 'skin' shows the loss due to the skin-effect in the DM circuit for a DM current of 1 A.

The radiated power from the DM circuit varies in an complicated way when the dielectric is present. Nevertheless, over the whole frequency range the DM-radiated power is much smaller than the 'Joulian loss' and therefore it can be neglected in the TL model. The same situation occurs when TL1 is open ended at side B.

The upper curve for the CM-radiated power loss (curve $(\cdots)$, labeled '1'), calculated for $I_{CM} = 1$ A, dominates the skin-effect loss above approx. 150 MHz. In our PCB I_{CM} is induced by the DM circuit, and will be smaller. The DM-CM coupling is taken dominantly inductive (see also Sect. IIe), with the inductive term M (=24 nH/m for this 5 cm wide GP) given by Eq. (21) of Report I. In the worst case the relation $|I_{CM}| \approx \omega M \ell |I_1| / Z_{CM}$ holds, which is similar to the Bersier-setup (Fig. 2b) with the 150 Ω impedance replaced by a short. The relation $Z_{CM} = j\omega L_{CM} \ell$ holds when the self-capacitance C_{CM} of the CM circuit and resonances in the CM circuit are neglected. With these assumptions $|I_{CM}| \approx M/L_{CM}|I_1|$ holds; for our 5 cm wide GP $Z_{CM} = 260$ Ω/m and $L_{CM} = Z_{CM}/c_0 = 870$ nH/m (see Sect. II.e). The curve $(\cdots)$ labeled 'w' is the radiated power P_{CM} for this worst case I_{CM}. Above approx. 350 MHz the CM-radiated power from to the PCB proper becomes larger than the skin-effect loss.

This estimation is conservative since in reality the total impedance of the CM loop will be generally higher, e.g. when the GP is loaded by a cable. Therefore, in practical situations the CM-radiated power exceeds the skin-effect losses for higher frequencies than 350 MHz. Also, I_{CM} will normally decrease for wider GPs since M decreases. When the width of the GP ranges $0 \leq 2w \leq 20$ cm, we found that the radiated CM power of the GP equals almost the radiated power by a thin-wire antenna above an infinite perfectly conducting plane.

Manneback concluded [3, p. 103]: '... the effect of radiation upon electromagnetic waves propagation along transmission lines is quite negligible as compared to the effect of heat

dissipation in the wires.' This conclusion also holds for the CM radiation of a PCB up to approx. 350 MHz and for the DM radiation up to 1 GHz. Both limits hold approximately for more complicated PCBs with continuous ground planes.

d. Short-circuit case

All tracks are shorted against brass plate B (Fig. 1). Figure 5 shows the modules of the measured and calculated transfer impedances between circuit 1 and 2 Z_T(1-2) and 1 and 3 Z_T(1-3).

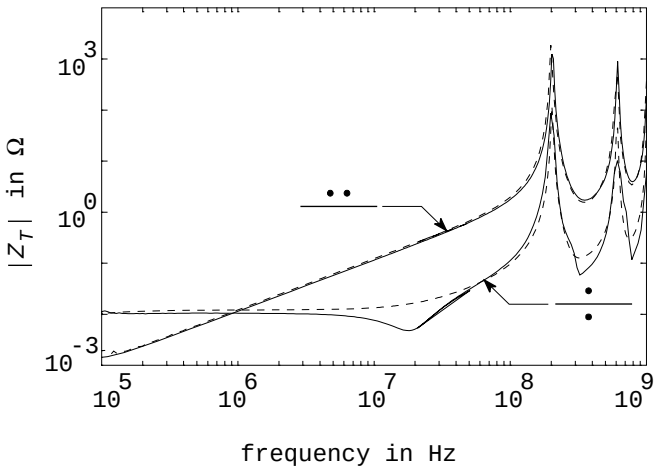

Fig. 5. Measured (—) and calculated (- - -) transfer impedances $|Z_T(1\text{-}2)|$ and $|Z_T(1\text{-}3)|$ for a $2w = 5$ cm wide GP; the tracks are shorted against brass plate B. Tracks 1 and 2 are on opposite sides at 5 mm from the middle line of the GP ($2w = 5$ cm); the x-distance between track 1 and 3 is $s = 10$ mm. The measured reduction of $|Z_t(1\text{-}2)|$ at 20 MHz is due to the skin effect in the GP (see Report I).

In the experiment the injected current I_1 and induced voltages V_{DMj} ($j = 2, 3, 4$), are all measured with an S-parameter set [23, Sect. VII]. The sensing circuit j is loaded by 50 Ω during the S_{j1} measurements. When these S-parameters are transformed into Z-parameters, the current I_j must be zero. Therefore, in our model (without TL5) the near-end impedances Z_{Aj} ($j = 2, 3, 4$) are all infinite; in the actual calculations 1 MΩ impedances were used. The far-end impedances Z_{Bi} ($i = 1, \cdots, 4$) are of course zero.

In the calculations we first used Collin's approximation for the skin-effect resistance (see Sect. II.b). Then the peak value of $|Z_t|$ at the first resonance ($\approx$ 200 MHz) was 10 dB too high for the tracks 1 and 3 on the same side of the GP, and 26 dB too high for the coupling to the other side. Three possible explanations were examined: 1) losses due to CM radiation, 2) errors as a result from S into Z-parameter transformation, and 3) higher resistive losses than expected.

1) As explained in the previous subsection, losses due to common-mode radiation are negligible compared to skin-effect losses. This is certainly true for the first resonance peak (see Fig. 4).

2) In the transformation from S-parameters into Z-parameters, terms such as $(1-s_{ii})$ occur in the denominator. For example, the input impedance of a single TL is $Z_{in} = (1+s_{11})/(1-s_{11})$, where s_{11} is near unity for a short-circuited TL. However, we found that the difference in the peaks could not be attributed to inaccuracy of the S-parameter measurements.

3) When we increased *ad hoc* the skin-effect resistance $R_s(\omega)$ for all frequencies by a factor five compared to Collin's value, the first peak is correctly described. The same factor also described the calculated $s_{12} = s_{21}$ parameters accurately. We believe that the relative high $R_s(\omega)$ is mainly responsible for the extra damping. In literature an increase in $R_s(\omega)$ of 50 to 100 percent is reported to be due to surface roughness. Our increase of 500 percent may be attributed to the manufacturing process. With this large factor 5 the CM-radiation losses become even less important compared to the skin-effect losses. Therefore, the 350 MHz limit stated in the conclusions of the previous subsection will shift to a higher frequency.

With the increased resistance, calculations and measurements agree very well. The peaks in $|Z_T|$ correspond to quarter wavelength resonances: $\ell = (2n+1)\lambda/4$ with $n = 0, 1, 2, ...$ Here λ is the wavelength calculated with Eq. (4) and $\varepsilon_{r,eff} = 3.34$.

e. Characteristic-termination case

When all tracks at the far end are terminated into their characteristic impedance of 68 Ω, the resonances in $|Z_T|$ will be strongly damped. As already mentioned in Sect. II.a, the DM-CM coupling modeled by TL5 must now be incorporated.

For a free standing PCB with no nearby conductor in parallel, the CM current returns as displacement current; the CM circuit is then difficult to describe. We took an inductive mutual coupling M_s [23, Eq. (21)] between the DM circuits $1, \cdots, 4$ to the CM circuit. For the return of the common-mode current we chose a large cylinder of radius $R = 1$ m. The mutual-capacitance $C_{s\infty} \approx 0.2$ pF/m from the DM tracks to this cylinder was numerically calculated by means of the method in Appendix A. The self-inductance L_{CM} and self-capacitance C_{CM} of the CM circuit follow from expressions for a strip $2w$ in a cylinder of radius R [41, Eq. (26.47)]

$$Z_{CM} = \sqrt{\frac{L_{CM}}{C_{CM}}} = \frac{\eta}{2\pi} \ln \frac{2R}{w}, \tag{12}$$

with $\eta = 120\pi$ Ω; for our 5 cm wide PCB this impedance becomes approx. 260 Ω. Further, we assumed *ad hoc* the near-end impedance $Z_{A5} = 0$ Ω and the far-end impedance $Z_{B5} = 377$ Ω, the free-space wave impedance.

The 5×5 $\mathbf{L}^*$ and $\mathbf{C}^*$ matrices become

$$\mathbf{L}^* = \begin{bmatrix} & & & & M_s \\ & \mathbf{L} & & & M_s \\ & & & & M_s \\ & & & & M_s \\ M_s & M_s & M_s & M_s & L_{CM} \end{bmatrix}, \tag{13}$$

and

$$\mathbf{C}^* = \begin{bmatrix} & & & & -C_{s\infty} \\ & \mathbf{C} & & & -C_{s\infty} \\ & & & & -C_{s\infty} \\ & & & & -C_{s\infty} \\ -C_{s\infty} & -C_{s\infty} & -C_{s\infty} & -C_{s\infty} & C_{CM} \end{bmatrix}, \tag{14}$$

with $\mathbf{L}$ and $\mathbf{C}$ the DM-DM matrices (Sect. II.b); $L_{CM} = Z_{CM}/c0 = 870$ nH/m and $\mathrm{diag}(\mathbf{L}) = (L_s, L_s, L_s, L_s)$, $L_s = 414$ nH/m. Since the diagonal elements of $\mathbf{C}$ are much larger than $C_{s\infty} \approx 0.2$ pF/m, the mutual-capacitance $C_{s\infty}$ is not added to these diagonal elements.

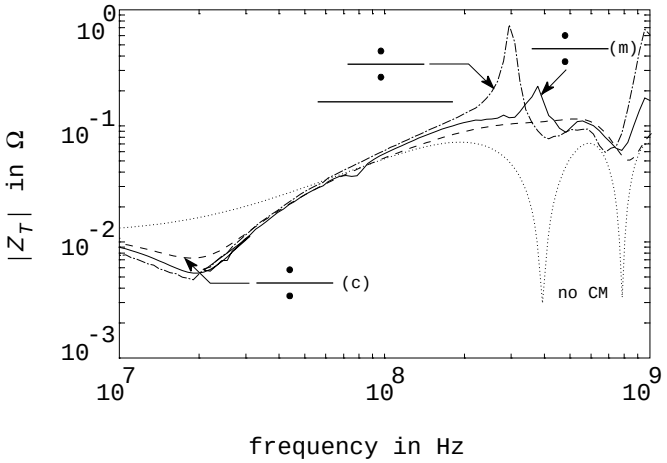

Fig. 6. Measured (—) and calculated (- - -) transfer impedance $|Z_T(1\text{-}2)|$ with 68 Ω termination; curve $(\cdots)$ gives the calculated $|Z_T(1\text{-}2)|$ neglecting the indirect DM-CM-DM coupling, i.e. without CM circuit or without TL5 in Fig. 3. For comparison we included the measured $|Z_T|$ with a metallic plate at a distance of 5 cm from the PCB $(- \cdot - \cdot -)$, see main text.

In Fig. 6 the transfer impedance $Z_T(1\text{-}2)$ is given for a free standing PCB. Since we are mainly interested in the HF behavior, we only show the frequency range 10 MHz – 1 GHz. Measurements (—) and calculations (- - -) agree well. In the experiments brass plate B was removed. The calculated Z_T without CM circuit (TL5 in Fig. 3) is given by curve $(\cdots)$ for comparison.

A large brass plate was placed at a distance of approx. 5 cm parallel from the GP and in contact with brass plate A. The CM circuit is now well defined. Curve $(-\cdot-\cdot-)$ is the measured $Z_T(1-2)$ for this situation. The nearby GP strongly reduces the mutual inductance and the mutual capacitance between the tracks; the indirect coupling DM-CM-DM now dominates Z_T.

III. HF effect of the DM-CM/Bersier structure

In this section we discuss the Bersier-like setup of Fig. 2a; the cross section is given in Fig. 7.

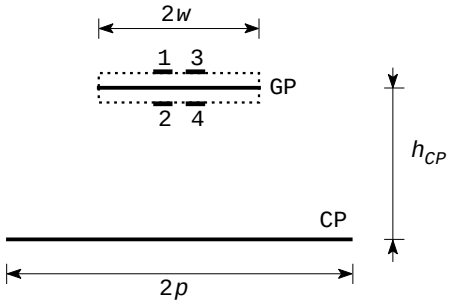

Fig. 7. Parameters for the PCB above a cabinet panel (CP).

The model (Fig. 3) for the DM-DM crosstalk with CM circuit included can also be applied

here. The nearby cabinet panel (CP) acts as a proper return path for the CM current through the PCB.

Transmission line parameters

The impedances Z_t(DM-CM) (per unit length) were treated in Sect. IV of Report I. An approximate analytical solution for the self-inductance L_{CM} of the CM circuit is given by Kuester and Chang [42] when $2w/h_{CP}$ is large. The capacitive coefficients can be calculated numerically with the method given in Appendix A. The DM-DM capacitive couplings become negligibly small, except those between the traces which are on the same side of the CP: between 1 and 3 and between 2 and 4. The DM-CM capacitive coupling coefficients are important and must be calculated with precision. We found an analytical approximation similar to the one in Sect. II.b, with the square root of $\varepsilon_{r,eff}$ replaced by the fourth root. Consider for example Fig. 7 with only track 1 present and the GP as reference. The inductance matrix $\mathbf{L}$ becomes

$$\mathbf{L} = \begin{bmatrix} L_s & M \\ M & L_{CM} \end{bmatrix}, \tag{15}$$

with L_s the microstrip self-inductance and M the mutual induction calculated by means of conformal mapping as discussed in Report I. Without dielectric, the capacitance matrix $\mathbf{C_0}$ follows from Eq. (9). The capacitive coupling C_{1-CP} with dielectric can be approximated by

$$C_{1-CP} \approx \frac{C_{1-CP,0}}{{\varepsilon_{r,eff}}^{1/4}}. \tag{16}$$

This procedure is again tested for a wide range of parameters. For a maximum deviation of 25 percent between numerical results and approximate analytical expressions this parameter range is: $1 \leq \varepsilon_r \leq 12$, $0 \leq x/2w \leq 0.9$, $0.5 \leq b/h \leq 3$, $0.05 \leq w/p \leq 1$, and $0.1 \leq 2w/h_{CP} \leq 3$.

The near end impedances (Fig. 3) Z_{Ai} $(i = 1, \cdots, 4)$ are all infinite; Z_{A5} is zero. The far end impedances Z_{Bi} $(i = 1, \cdots, 4)$ are zero for the short-circuit or 68 Ω for the characteristic-termination case. The input capacitances of CMOS circuits are usually a few pF; in a first approximation Z_{Bi} was also taken infinite.

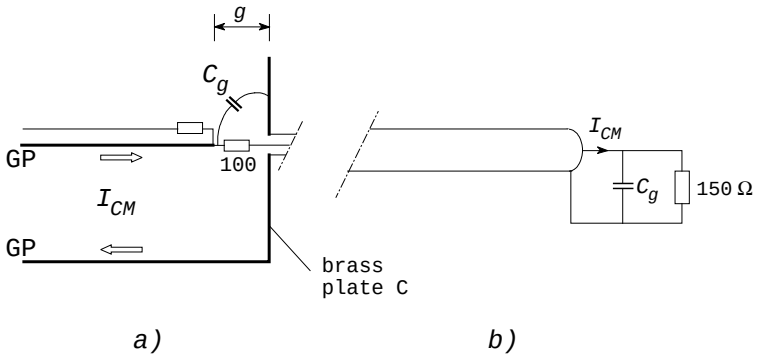

Fig. 8. a) Gap g between the GP and brass plate B; the capacitance C_g across this gap is schematically given in the figure. b) Equivalent model for the CM part of the TL model.

Gap capacitance

The far-end impedance Z_{B5} in the CM circuit was 150 Ω, a 100 Ω resistor in series with the 50 Ω input impedance of the measuring equipment. Experiments showed that the capacitance C_g between the GP and the brass plate C (Figs. 2a and 8) becomes important above 100 MHz for smaller width of the gap g; Z_{B5} is made up of the 150 Ω resistor with C_g in parallel. Only the part of the CM current flowing through the 150 Ω is measured.

Figure 9 shows the measured current ratios I_{CM}/I_1 and I_{CM}/I_2 when a DM current is injected in track 1 (I_1) or in track 2 (I_2); the widths of the gaps were 1 cm (solid lines) and approx. 0.5 mm (dashes).

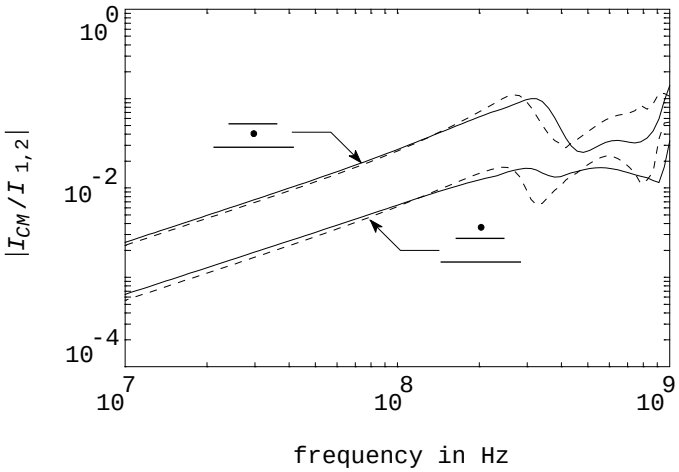

Fig. 9. Measured current transfer between DM and CM circuits. The DM track was either above or below the $2w = 5$ cm wide GP. The setup is given in Fig. 2a; the DM tracks were terminated in 68 Ω. Curve (—) corresponds with a $g = 1$ cm long gap (Fig. 8) and (- - -) corresponds with $g \approx$ 0.5 mm.

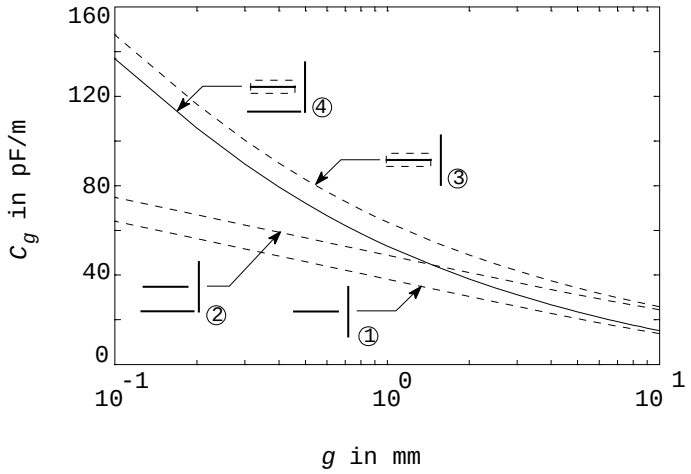

Fig. 10. Calculated capacitance C_g for different configurations: (1) Ground plane GP (see Fig. 8) at a distance g from the vertical brass plate C of height 2 cm, no CP present. (2) The same as (1) but with a 20 cm long CP at a distance $h_{CP} = 1$ cm below GP. (3) PCB coated with a dielectric $\varepsilon_r = 4.7$ at a distance g from plate C. (4) The coated PCB with plates CP and C.

We calculated C_g with the method of Appendix A for different configurations; see Fig. 10. The dielectric layer of the PCB increases C_g and the vicinity of the cabinet panel CP lowers it. For our 5 cm wide GP and a gap of approx. 0.5 mm the capacitance $C_g = 3.5$ pF. Fitting the model to the measurements, we found $C_g \approx 10$ pF for the 0.5 mm gap. The deviation is probably due to fringing fields. Note that $\omega R C_g \approx 10$ at 1 GHz for the narrow gap, with R the 150 Ω CM resistor. From other experiments with small gap distances we learned that the value of C_g, 10-15 pF, only slightly depended on the width of the GP. In addition, measurements and calculations with gaps of about 0.5 mm showed that C_g affect the current ratio I_{CM}/I_{DM} mainly when the DM circuits are terminated into impedances larger than the characteristic impedance of 68 Ω. All measurements presented further down were performed with a $g = 1$cm long gap; then the effects of C_g can be neglected up to 1 GHz. This value of g is a compromise; larger gaps would increase the contribution of the 100 Ω resistor to the inductance in the CM loop.

Results for straight tracks

In Fig. 11 the current ratios I_{CM}/I_1 and I_{CM}/I_2 are given for the (DM) characteristic-termination case.

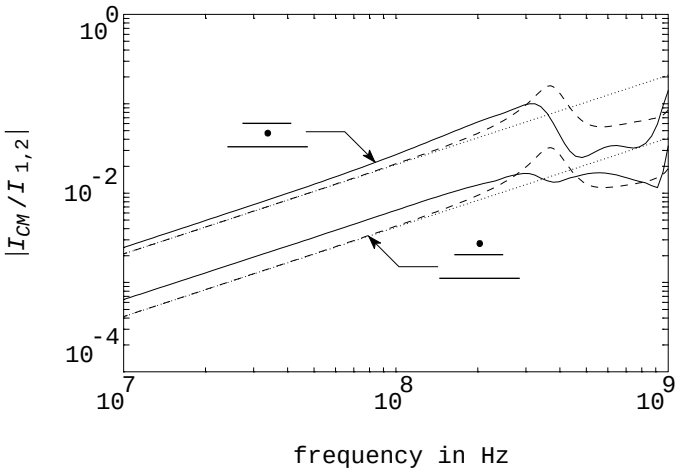

Fig. 11. Measured (—) and calculated (- - -) current transfer between DM and CM circuits of the Bersier setup (Fig. 2a); the tracks are terminated at the far end of the PCB into their characteristic impedances of 68 Ω. The approximation (17) is given by the dotted line.

Calculations and measurements correspond well. Observe that the curves for this case are approximately equal to (see also Fig. 2b):

$$\frac{I_{CM}}{I_{1,2}} = \frac{Z_T(\omega) I_{1,2}/150}{I_{1,2}} = \frac{j\omega M_{s1,2}\ell}{150}, \tag{17}$$

since $Z_T(\omega) \approx j\omega M_{s1,2}\ell$; see curve $(\cdots)$ in Fig. 11.

Figure 12 shows the current ratios for the short-circuit and open (infinite termination) case. The markers show the resonance-frequencies f_{rDM} where the input-current $I_{1,2}$ is minimal and f_{rCM} where the common-mode circuit resonates. For the shorted case $f_{rDM} = 200$ and 600 MHz and $f_{rDM} = 400$ and 800 MHz with open ends. In both cases $f_{rCM} = 375$ and 750 MHz.

Again, the calculated and measured curves correspond well. Note that at the resonance frequencies the CM current becomes equal in magnitude to the injected DM current.

Figures 11 and 12 show clearly the effect op the position of the DM circuit and the termination of it. In order to comply with the emission norm, measures must be taken for modern digital circuits. With short-circuited or open-ended DM circuits the EMC measures must be more extensive since at resonances large CM currents will flow. For digital electronics one should avoid the excitation of these resonances.

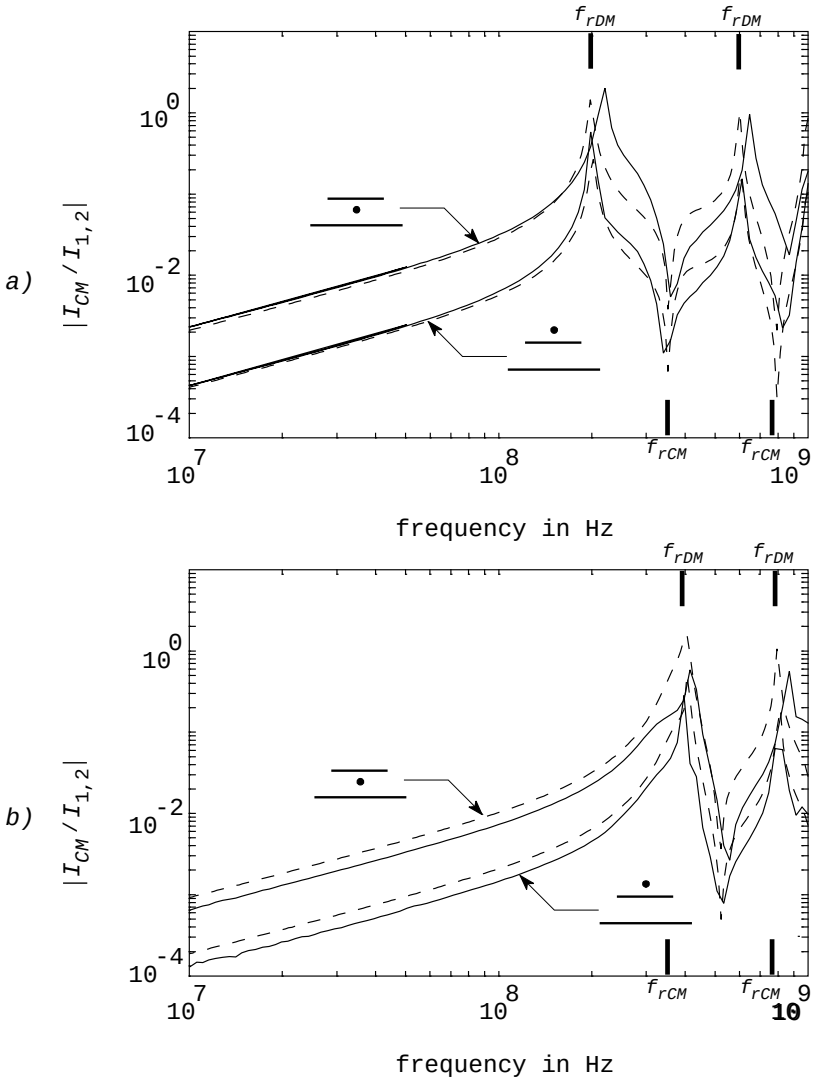

Fig. 12. Measured (—) and calculated (- - -) current transfer between DM and CM circuits of the Bersier setup (Fig. 2a). The tracks are a) shorted and b) opened at the far end of the PCB. The markers f_{rDM} and f_{rCM} show the resonance frequencies in the DM and CM circuits, respectively.

IV. More complicated tracks

The TL method appeared to work quite well for straight tracks. We now address more complicated tracks as on practical PCB's. Many experiments were carried out; we selected for presentation those which we consider to be a critical test of the TL method and its limits of validity. In the simple PCB_1 (Fig. 13a) tracks 1 has only two bends; on PCB_2 (Fig. 13b) track 1 meanders over the PCB. Both PCB's were 10 cm wide and had a length $\ell = 20.5$ cm.

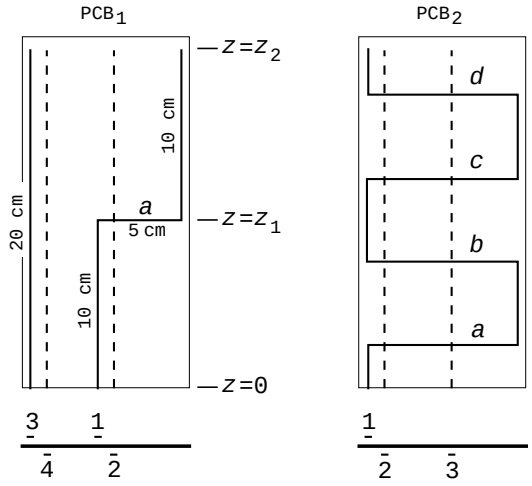

Fig. 13. Two demonstration boards, PCB_1 and PCB_2. Solid lines correspond to the upper layer of the PCB; dashed lines to the lower layer. The GP is the middle layer, with width $2w = 10$ cm and lengths 20.5 cm; the straight tracks are $\ell = 20$ cm long.

a. DM to CM crosstalk

The Bersier setup has already been discussed in the previous section; see Fig. 2a. Current is again injected in track 1.

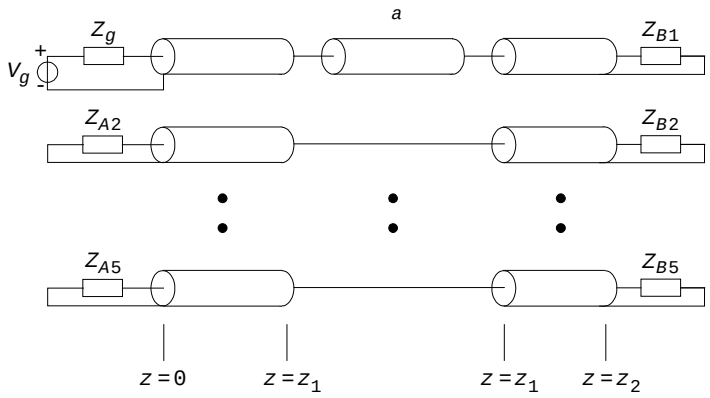

Fig. 14. Transmission-line model for the Bersier-setup of Fig. 2a with PCB_1. TL1-TL4 corresponds to the tracks on the PCB, while TL5 represents the CM circuit.

Figure 14 shows the TL model for PCB_1, which is similar to the one of Fig. 3, with TL a added to describe the extra length a of track 1 in Fig. 13a. Part a is perpendicular to the

other tracks and the CM circuit; only a negligibly small inductive coupling is expected, or none at all. We also disregard the capacitive coupling of part a. The coupling parameters of the rest of track 1 are calculated as discussed in Sects. II and III. Figure 15 shows the measured and calculated current transfer between DM and CM circuit, for all DM tracks at the far end shorted, $Z_{Bi} = 0$, or terminated $Z_{Bi} = 68\ \Omega$ $(i = 1, \cdots, 4)$.

The first peak in Fig. 15a at $f = 160$ Mhz corresponds with a quarter-wavelength resonance of the injection track 1 with total length $\ell_1 = 25$ cm.

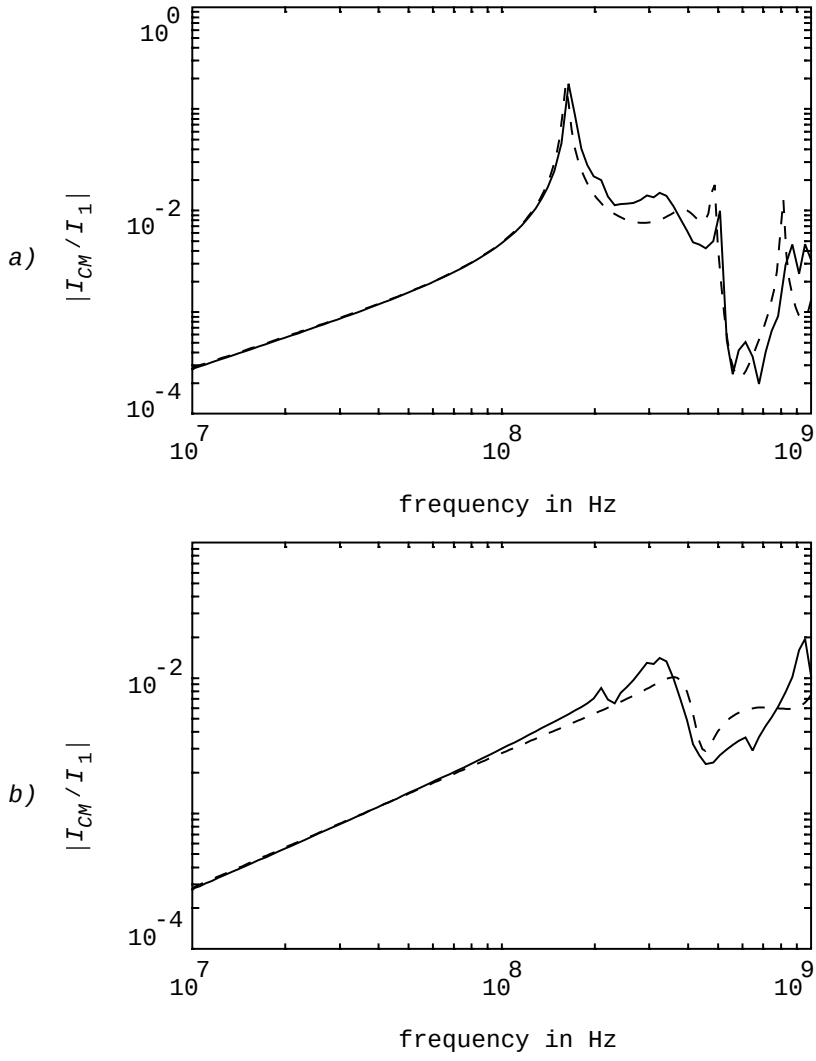

Fig. 15. Measured (—) and calculated (- - -) ratio of common-mode current to injected current of PCB_1 with shorted tracks (a) and characteristic terminated tracks (b), i.e. $Z_{Bj} = 0$ and $Z_{Bj} = 68\ \Omega$, respectively $(j = 1, \cdots, 4)$.

The results for PCB_2 with $Z_{B1} = \infty$ and $Z_{B1} = 68\ \Omega$ are shown in Fig. 16. The orthogonal tracks $a, \cdots, d$ are modeled in the same way as a of PCB_1. The first peak in Fig. 16a at $f \approx 140$ MHz corresponds with a half-wavelength resonance on track 1, now of length $\ell_1 = 56$ cm. The simple TL method becomes less accurate above approx. 400 MHz. The frequencies of the resonances are still correctly calculated, but their amplitudes disagree by an

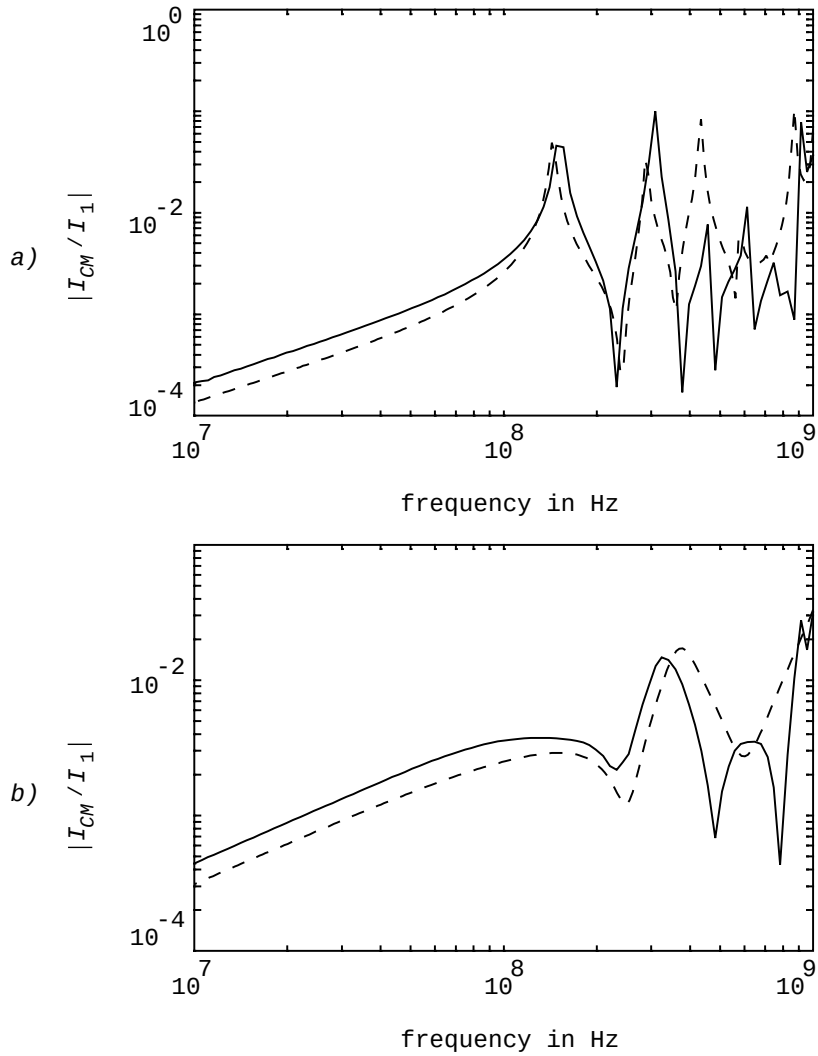

Fig. 16. a) Measured (—) and calculated (- - -) current ratio I_{CM}/I_1 of PCB_2 with open ended tracks. b) The same with 68 Ω terminated tracks.

order of magnitude. Fortunately the calculated curve is higher for almost all frequencies above 400 MHz, and can therefore be used as a first-order approximation in practical applications. Clearly a more elaborate model would be required; we presume that the capacitive coupling between the parts $a, \cdots, d$ and the CM circuit should be included first. This however lays outside the scope of this report.

b. DM-DM crosstalk

As stated before, the DM-DM crosstalk is an even more critical test since the coupling terms are small. In Fig. 17 we present the DM-DM transfer impedance Z_T(1-2) for the free standing PCB_1 with tracks shorted (s) or terminated in 68 Ω (t). The CM circuit (TL5 in Fig. 14) is formed by the GP and a return at large distance (Sect. II.e), with only inductive couplings from the parallel tracks to this return. Again, the inductive coupling from the orthogonal track a to the return is disregarded. The treatment is further the same as for the straight-track

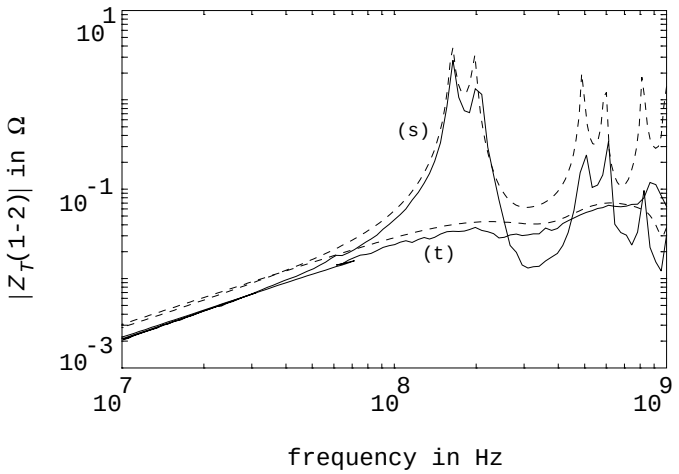

Fig. 17. Measured (—) and calculated (- - -) DM-DM transfer impedance $|Z_T(1\text{-}2)|$ for PCB_1 with shorted (s) and 68 Ω terminated (t) tracks.

problem in Sect. II.

The peak of $Z_T(1\text{-}2)$ at 160 MHz for the shorted tracks correspond with the quarter-wavelength resonance of track 1 with total length $\ell_1 = 25$ cm; the peak at 200 MHz with the corresponding resonance of the sensing track 2 with length $\ell_2 = 20$ cm. The $Z_T(1\text{-}2)$ and $Z_T(1\text{-}3)$ results for PCB_2 (short-circuit case) are shown in Fig. 18.

Observe that the measured curve is higher than the calculated. A large deviation occurs in $Z_T(1\text{-}2)$ at the peaks at $f \approx 200$ MHz and $f \approx 700$ MHz. For $Z_T(1\text{-}3)$ the correspondence was much better. Probably the capacitive coupling of the relative long orthogonal tracks $a, \cdots, d$ has a significant influence when the direct coupling of the parallel tracks is small.

c. Additional remarks

Some experiments were done with loops in the injection circuit where the straight track 1 (Fig. 1) was raised by 5 mm above the GP over 2 cm length. These loops model ICs and connectors and are represented in the calculations by local mutual inductive couplers. Measurements and calculations corresponded well for this (simple) DM-DM case.

We also studied the effect of the brass plates on the transfer impedance Z_T in the DM-DM case. In the experiments we removed brass plate B (Fig. 1). These experiments showed that only the d.c. part changed significantly. For completeness a theoretical derivation for this transfer resistance is given in Appendix C.

From the previous subsection it follows that the simple TL model is somewhat limited in use for the DM-DM crosstalk. That is, when tracks are on opposite sides of a three layer PCB and the orthogonal tracks are larger than the parallel tracks. Nevertheless, the TL method gives good results when the tracks are on the same side where the couplings are much larger.

Observing the Figs. 15 and 16, one may conclude that the simple TL model for the Bersier-like setup works quite well up to approx. 400 MHz. Above this frequency the model is certainly useful as a first-order approximation, because then our TL model predicts the CM current too high. As pointed out in the Introduction, this DM-CM coupling is important in practical situations; a somewhat higher calculated value for I_{CM} may serve as a warning to the designer.

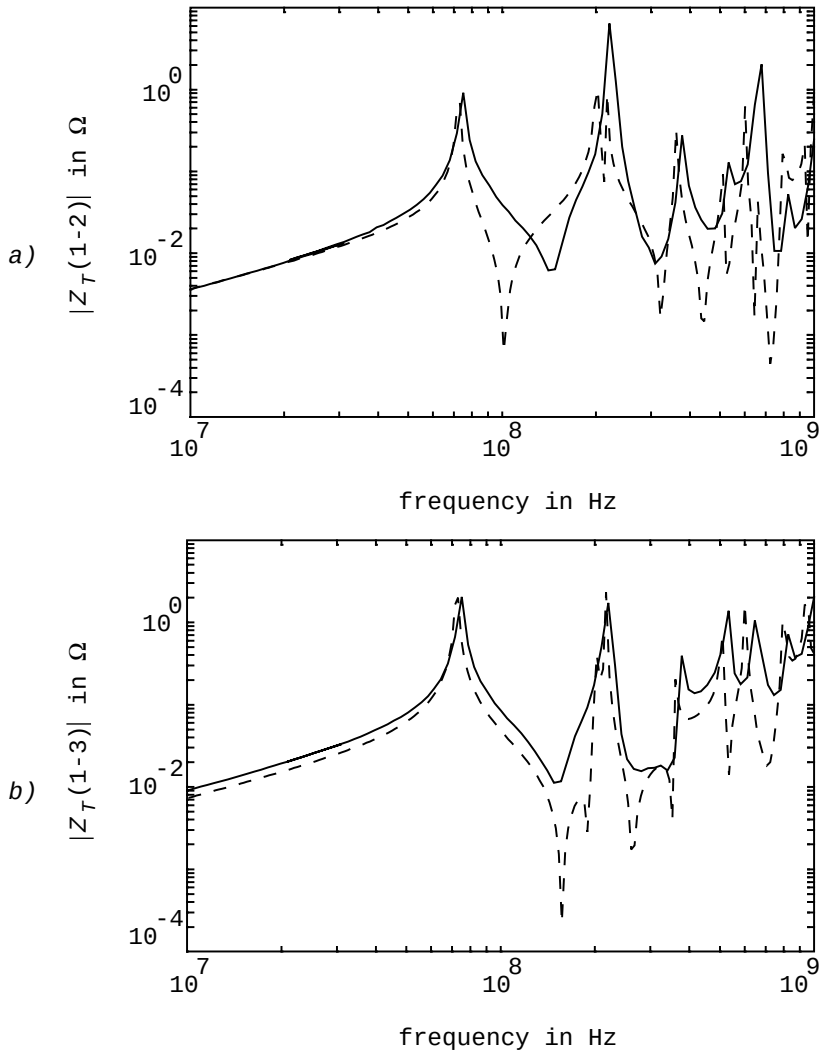

Fig. 18. Measured (—) and calculated (- - -) DM-DM transfer impedance $|Z_T(1\text{-}2)|$ and $|Z_T(1\text{-}3)|$ for PCB_2 with shorted tracks.

V. Implementation into a design stage

Our method is suitable for incorporation in the design stage of a product; a possible design-flow diagram is shown in Fig. 19. The most important object is avoiding the large feedback from the prototype to the layout/placement process, since changes in the design after prototyping are expensive. The following gives a global implementation-schema of our method in the design stage.

The design process starts with an idea, a functional design, and a functional simulation. These steps are still independent of the board technology. After a successful functional simulation some initial choices have to be made, such as: PCB type (number of layers, VCC/GND layers), logic type (HCT etc.), cabinet (metal, plastic), connector type etc.

The physical design stage involves the component placement and routing. The delays in the components and along the tracks should not exceed certain limits, as can be verified by a signal-integrity analysis (SIA). It is advantageous to implement some EMC design rules and

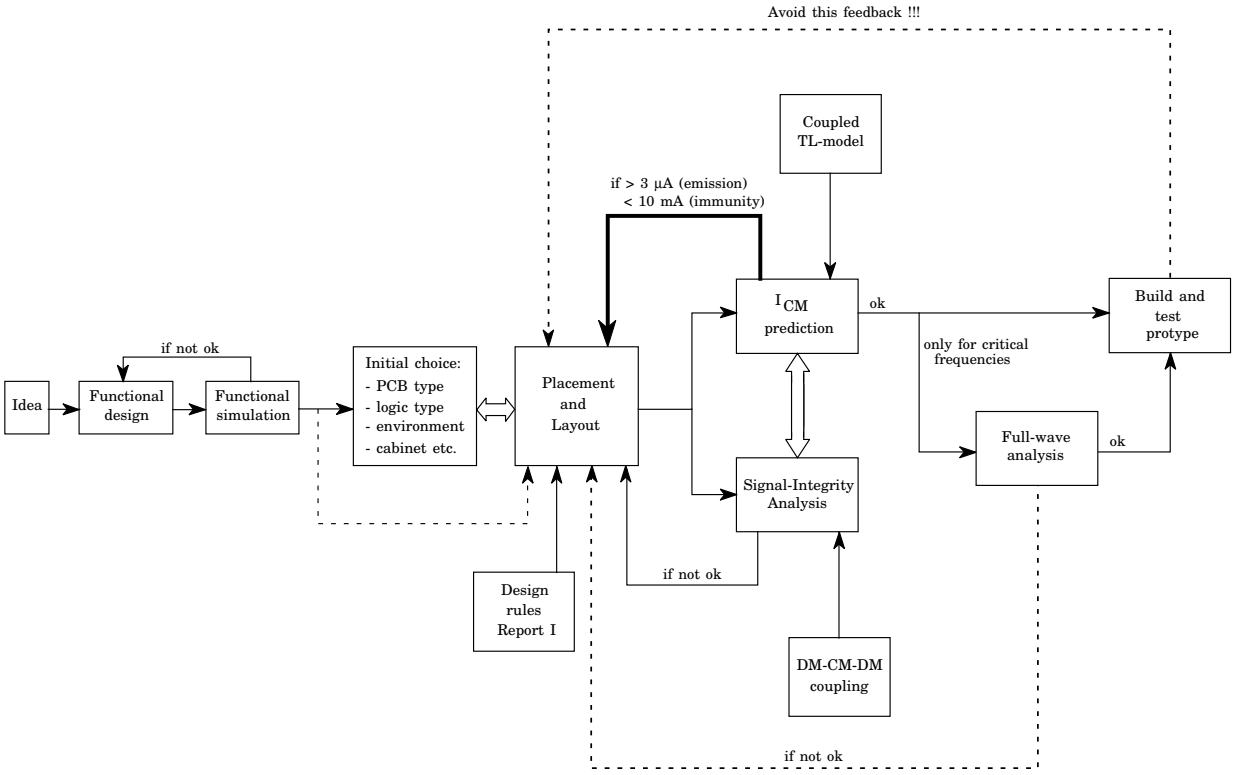

Fig. 19. A design-flow diagram of a product; for explanation see the main text.

formulas from Report I at this stage already. For example, the digital waveform parameters of a DM current through a straight track are known either from data-sheets or from the functional simulation. The mutual-inductive coupling from any track to the CM circuit could be monitored permanently during the routing of that track. The upper boundary for the CM generated by the current is then estimated by Eq. (39) of Report I. If the 3 μA emission rule is exceeded, a warning with possible solutions should be given. The DM-CM-DM coupling (Sect. II.e) should be included in the SIA. The reciprocal situation, i.e. current injection, can also be analyzed with the TL model when the DM loads are linearized.

The SIA and I_{CM}-prediction can be performed in parallel. To this end one adds the CM circuit to the coupled TLs for the interconnects which are needed in the SIA anyhow. Only if the SIA gives no problems AND the emission (3 μA) and immunity (10 mA) EMC requirements are fulfilled, an actual prototype can be considered. For frequencies where the EMC rules are critical, a further full-wave analysis could be performed. However, the feedback from the time consuming full-wave analysis to the placement/routing process is often not necessary.

The last step in the design process is building and testing the prototype. Practical experience shows that the product usually complies with the regulatory EMC requirements when the precompiance EMC rules are fulfilled.

VI. Demo boards with digital logic

Practical printed circuit boards can be very complex. In order to keep the bookkeeping effort acceptable, two digital boards were designed as demonstration boards. The functional design is given in Fig. 20 whereas figure 21 shows the layout of the 10 cm wide boards for HCT and HLL digital logic. Only the more important DM-CM coupling will be considered.

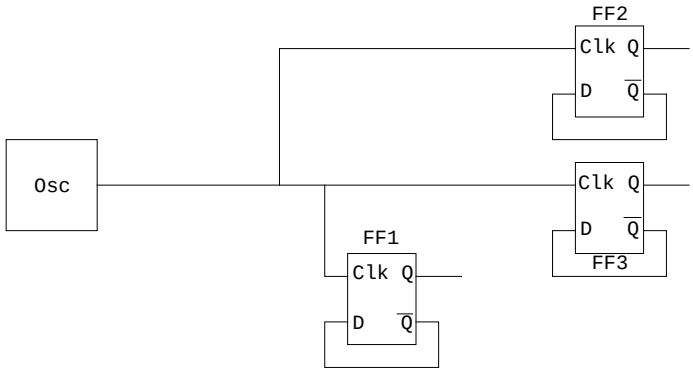

Fig. 20. Functional design for the digital boards shown in Fig. 21.

a. Description of the boards

Each board contains three D flip-flop (FF) ICs: 74HCT74 and 74HL33534. We use one FF of each IC; the HCT types were placed on sockets. The TTL compatible quartz crystal oscillators (OSC, Fig. 20) had fundamental frequencies of 10 MHz, 20 MHz, 50 MHz, and 100 MHz (the last one only for the HLL board). The external voltage of approx. 15 V was reduced on the boards by 7805 and TLV2217-33 voltage stabilizer with decoupling capacitors placed in their near vicinity. The pads in the supply tracks were intended for SMD common-mode chokes. The SMA connector for the external supply was on the same panel as those for the DM circuits 1, 2, and 3. Since HLL logic requires 3.3 V and the oscillator 5 V, two supplies were needed for the HLL board; a translator T (74HL33244) transformed the 5 V oscillator output into a 3.3 V signal. Each supply pin was decoupled to the ground plane by a 22 nF decoupling capacitor.

The sensor s with mutual inductance M_{sens} measured the DM current; the measured sensor output V_{sens} was integrated numerically, i.e. $I^m_{DM} = V_{sens}/j\omega M_{sens}$. In principle, only one place suffices for the I^m_{DM} measurement if the termination of the DM tracks is known and linear, since the TL model contains all forward and backward waves.

Time domain measurements were carried out with a 8 GSa/s HP 54720D/54721A digital scope (1.1 GHz bandwidth). In the spectral domain we used a HP 4396A spectrum analyzer. The resolution and video bandwidth (RBW and VBW) of the analyzer was in all measurements 30 kHz and the frequency span was 100 kHz – 1.82 GHz. The measurements with the scope and analyzer were consistent with each other, as was verified by a FFT on the time domain signal.

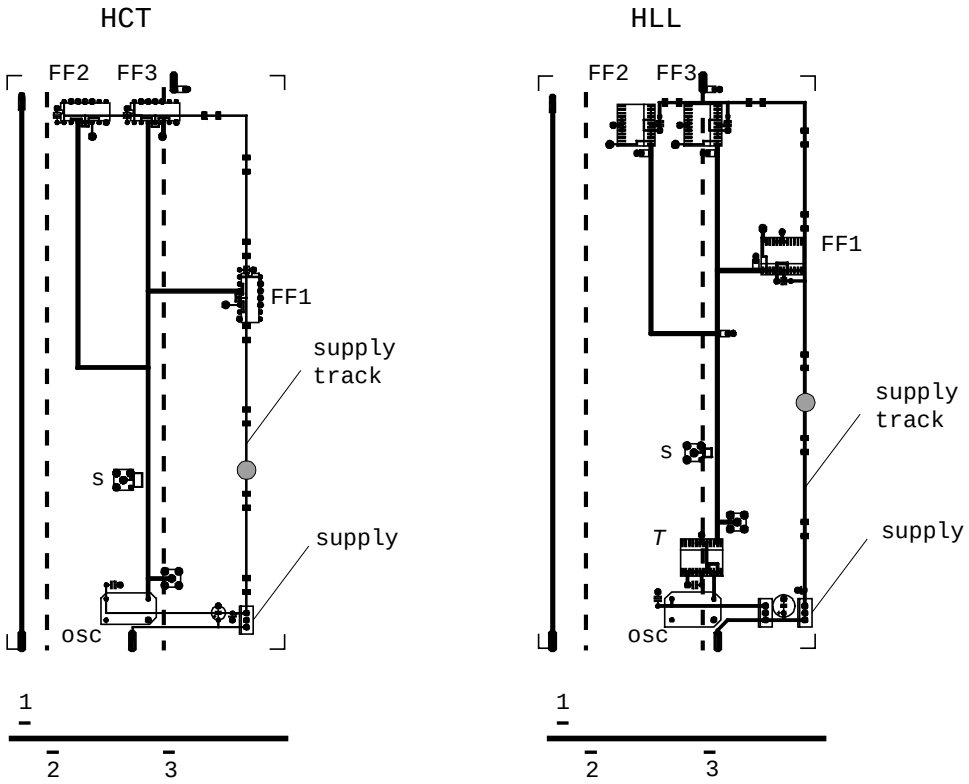

Fig. 21. HCT and HLL boards consisting of three D flip flops (FF) and a clock oscillator (OSC, see Fig. 20); for the HLL board an extra translator T was necessary (see text). The solid lines correspond to the upper layer of the PCB and the dashed lines to the lower layer. The DM currents were measured with inductive current sensors s, the mutual couplings between sensor and track were $M_{sens} = 0.97$ nH (HCT) and $M_{sens} = 0.29$ nH (HLL). The external voltage was regulated by on-board voltage ('supply') stabilizers (see also main text). The circles in the supply tracks show the positions of 7 mm wide and 9 mm high loops when the currents through these tracks were measured.

b. TL model and transfer function

The transmission-line model has been discussed in Sects. II, III, and IV. The nonlinear devices are simplified/linearized to an IBIS (Input/output Buffer Information System) model. The output impedances (Z_g in Fig. 3) of the Thevenin equivalent models for the oscillator and the translator T were 20 and 12 Ω. The rise and fall times of the voltage source (V_g in Fig. 3) were about 2 ns for HCT and 1 ns for HLL; these parameters were obtained by separate measurements. For the far end impedances on the boards (Z_B's in Fig. 3) we assumed the input capacitances $C_i = 3.5$ pF for both logic types. Some nonlinearity of the capacitance could occur due to the Miller effect inside the ICs; this was neglected in the calculations.

We first assume a voltage source $V_g = 1$ at the position of the oscillator or translator, with proper output impedance; we then determine the differential-mode current I_{DM} at the position of current-sensor s. We calculate the transfer function $H(\omega) = I_{CM}/I_{DM}$ at many frequencies, where I_{CM} is the calculated current through the 150 Ω impedance (Fig. 2a).

c. Common-mode current

Figure 22a shows the measured (—) and calculated (o) spectrum of the common-mode current I_{CM} for the HCT board with 50 MHz oscillator. The I_{CM} calculation is based on the actual I^m_{DM} measured with current sensor s, i.e. $I^m_{CM}(\omega) = H(\omega)I^m_{DM}$. The noise level between the peaks in the I_{DM} measurements was nearly constant; the nearly continuous lower line of the calculated curve (o) is this DM noise level times the transfer function $H(\omega)$. Therefore, the transfer function is implicitly shown in the figure.

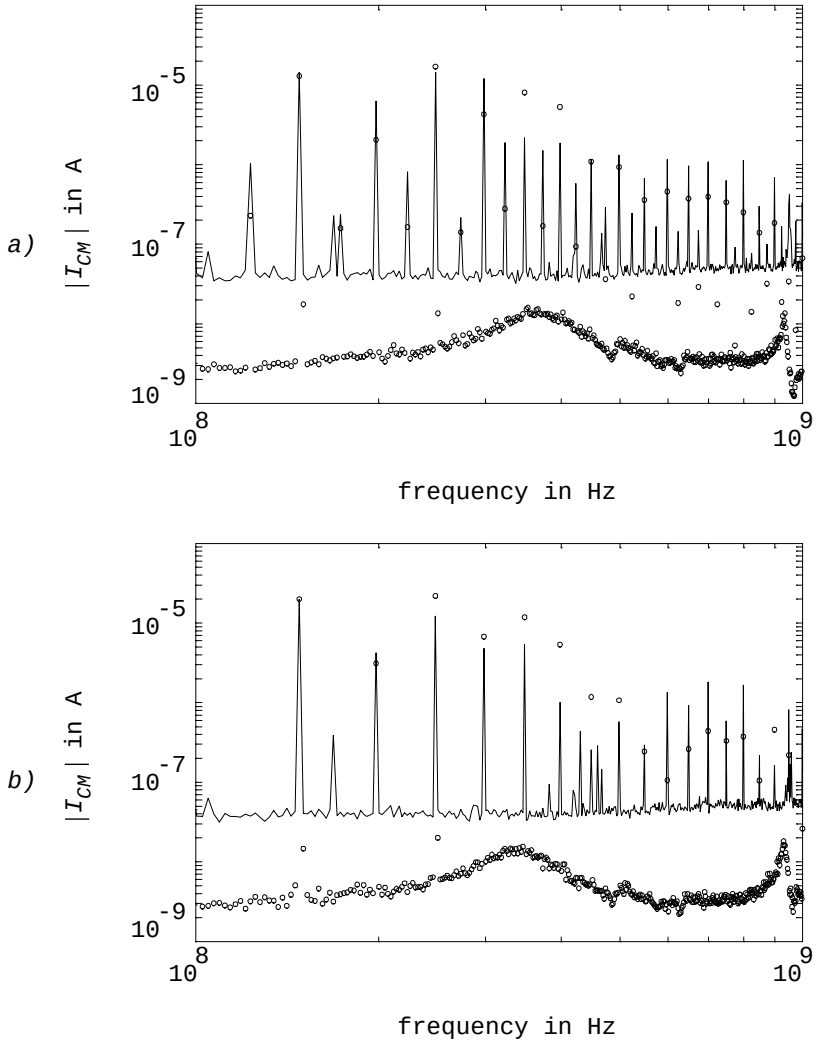

Fig. 22. a) Measured (—) and calculated (o) spectral component of the common-mode current I_{CM} in the Bersier setup for the HCT board with 50 MHz clock speed and b) measured (—) and calculated (o) I_{CM} with the ICs removed out their sockets. The lower line (o) shows implicitly the transfer function $H(\omega)$.

Measurements and calculations agree in the mean to within approximately 8 dB for the harmonics of the clock, with a maximum deviation of 15 dB at a few frequency components. A similar behavior was observed for the other oscillators and the HLL board. From these observations we conclude that the TL approach is applicable for the HCT board up to approx. 700-800 MHz, and for the HLL board up to approx. 1 GHz. For the HCT board the procedure

breaks down at a lower frequency, which is probably caused by the additional inductive coupling of the HCT ICs on their high sockets.

Since the FFs act as dividers, subharmonics are present in the measured CM current. The even terms of these subharmonics add up to the harmonic components. Figure 22b shows the measured CM current with the ICs removed: the subharmonics disappear. A careful comparison between Figs. 22a en 22b shows that the even terms of the subharmonics do not have a significant influence on the harmonic components. The peaks at $f \approx 160$ MHz and around 450 MHz are due to external fields caused by mobile communication; we did not use a shielded room.

The calculated subharmonics in I_{CM} are always lower than those measured. The subharmonics in I_{CM} are not caused by the signal track, since there is a good correspondence for the harmonics. We investigated the subharmonic contribution from the supply track, first by direct measurement of the DM current and secondly by placement of SMD common-mode chokes [43] between the pads.

1) The supply-track current was measured with a Tektronics P6022 current-probe in the frequency range 10 MHz – 200 MHz. For this purpose a 7 mm wide and 9 mm high loop was placed in the supply track at the position indicated by a circle in Fig. 21. At any frequency the supply-track current was more than 20 dB lower than the DM current for the HCT board, and approx. 40 dB lower for the HLL board. Since the mutual inductive couplings to the CM circuit is about the same for signal and supply tracks, the supply-track current cannot be the source for the subharmonics. Observe also the effect of the decoupling capacitor on the supply-track current: since the loop formed by this capacitor and the V_{CC}-pin/GND-pin at the IC is smaller for the HLL board than the HCT board, less current will flow in the HLL board compared to HCT.

2) Supply track chokes with self inductances of 470 nH did not decrease the subharmonics in the CM current (both boards). Since the chokes are very small, the extra mutual couplings from the chokes to the CM circuit can be neglected. The chokes indeed decreased the supply-track current in the frequency range 10 MHz – 200 MHz.

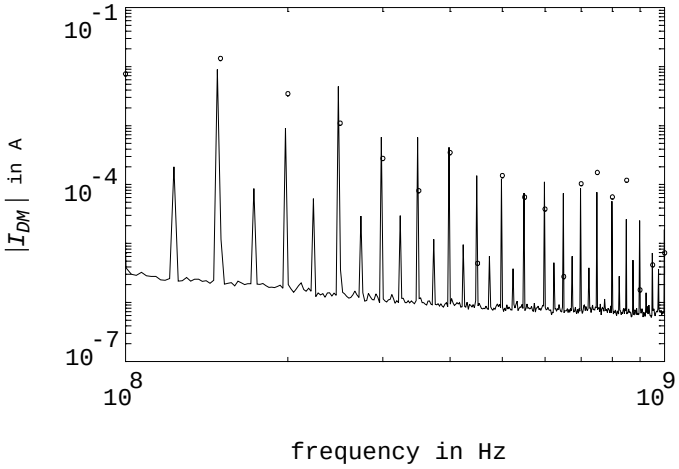

Fig. 23. Measured (—) and calculated (o) DM current for the 50 MHz HCT board.

No further attempts were made in order to find the coupling for the subharmonic generation in the CM current. Nevertheless, for the first few spectral components the harmonics

are much larger than the subharmonics. Therefore, in this case the harmonics are the most important one.

d. Differential-mode current

In the previous subsection the measured DM current was used in order to describe the CM current generation. Figure 23 shows the spectrum of the calculated and measured DM current (HCT, 50 MHz).

The agreement between calculations and measurements is good, except at the frequencies $f = 450,\ 650,$ and 900 MHz. A detailed analysis showed that the voltage to current ratio Z_{in} of the DM circuit seen at the position of sensor s, resonated strongly (see Fig. 24) near these frequencies. A small error in the calculated frequencies may then result in a large deviation of I_{DM} at the actual harmonics of the clock.

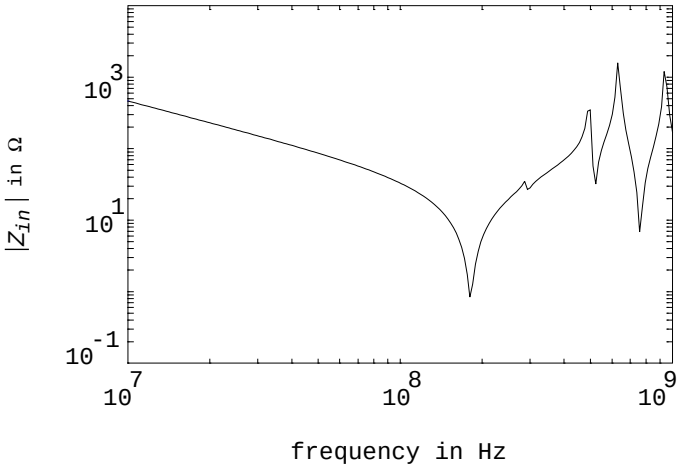

Fig. 24. Calculated voltage to current ratio Z_{in} in the DM circuit at the position of the sensor s.

A better model for the DM currents, which includes the subharmonics, should include the nonlinearity of the devices. First the properties of the lossy TLs are solved in the frequency domain; secondly, the nonlinear devices connected to the TLs are considered in the time domain, see Djordjević *et al.* [30, 44] for more details.

This approach sounds quite simple. For our HCT and HLL logic Spice models can be found indeed. However, in general an accurate description of the models does not exist for complex ICs. This problem is very important in any application of our method, since the lack of a good description of complex ICs can result in significant deviation between calculations and measurements. Of course, this problem remains when a full-wave approach is utilized instead of our TL method. This is our main reason to measure rather than calculate the DM current.

VII. Grounding structures

Up to now we considered continuous ground planes. As is generally known, PCB with ground tracks or with cuts in the GP are undesirable from an EMC point of view. Intertrack coupling as well as CM coupling is large. Nevertheless, such PCBs can be found in practical equipment. As a warning we give some results on test PCBs.

a. Grounding tracks

Fig. 25 shows the cross section of a three layer demonstration PCB with three DM tracks (1, 2, and 3) and two grounding tracks (4 and 5); all straight tracks were 20 cm long. The DM tracks were terminated at the far end with grounding track 5 into different impedances; the grounding tracks 4 and 5 were shorted at both ends. In the Bersier setup this structure was placed at $h_{CP} = 1$ cm above the CP.

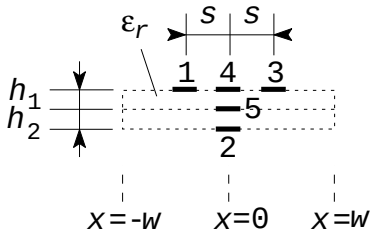

Fig. 25. Cross section of a $2w = 10$ cm wide PCB consisting of three DM tracks 1, 2, and 3, and two grounding tracks 4 and 5; the upper tracks were $s = 10$ mm separated and all tracks were of width $W_t = 1.5$ mm.

The **C** matrices (DM-DM and Bersier) were calculated with the method given in Appendix A. The inductance matrices follow from Eq. (9). In all cases track 5 was assumed as reference. The value of the skin-effect resistance was the same as in Sect. II.d.

Good correspondence between measurements and calculations was obtained for both the Bersier and the DM-DM setup. The deviation was always smaller than 10 dB. As a demonstration, Fig. 26 shows the Bersier results with a 470 Ω termination for tracks 1 and 3, and a 100 Ω termination for track 2. The characteristic impedances of these tracks against reference 5 were 426 Ω and 102 Ω, respectively.

With ground tracks rather than a ground plane, the electrical-field lines are strongly concentrated near the tracks. Hence, the fringing fields at the far end of the tracks are more pronounced compared to the fringing fields with a wide GP. In the model the terminations Z_{Bi} consisted of the resistors paralleled with stray capacitances of 1 pF (obtained by fitting). These fringing-field capacitances shifted the calculated resonances in the DM circuit to the correct value. Therefore, the sharp resonance at $f \approx 500$ MHz depends critically on the correct description of the DM circuit. Above this frequency the maximum deviation is approx. 9.5 dB; the calculated curve is again higher than the measured one.

b. Ground planes with cuts

Ground planes with cuts are of practical importance, although it is not advisable to allow such cuts. For example, analog and digital ground planes are often separated in order to avoid common-mode impedance coupling. Furthermore, the voltage generated over the 'effective inductance' of the ground plane by means of a current flowing through the plane, is commonly

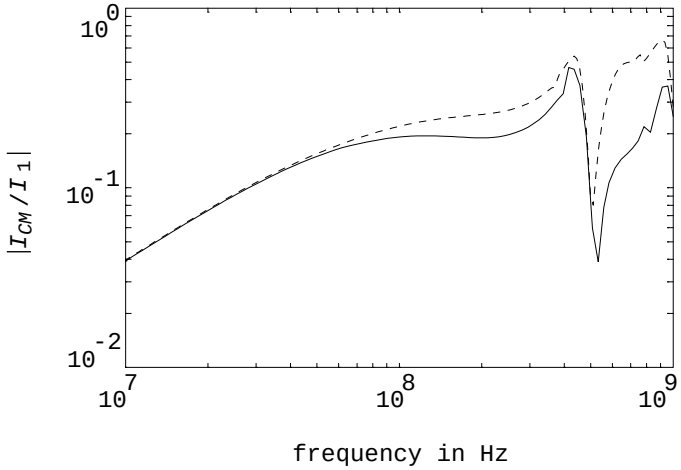

Fig. 26. Measured (—) and calculated (- - -) current ratio I_{CM}/I_1 for the 5 track problem of Fig. 25. Tracks 1 and 3 were terminated into 470 Ω resistors with track 4, while track 2 was terminated into a 100 Ω resistor with track 5; the three resistors were in the model paralleled with a stray capacitance of 1 pF at the far end B (see main text). The grounding tracks 4 and 5 were shorted at both ends.

seen as the source for driving the antennas (cables). Therefore, the cables are often connected to a separate 'quiet' or 'clean' ground plane (one not contaminated by the analog and digital noise); see Ott [9] and Paul [45, Sect. 13.3.3]. These GPs are connected with each other at single points. A common-mode current through these connections results in high couplings.

In this subsection a GP with a simple cut of different lengths is investigated, which is a simple example of the above mentioned 'separated' GPs. Fig. 27 shows the PCB structure for this special GP of length 20 cm; the tracks were $\ell = 20$ cm long. Again, tracks 1 and 3 are the upper layer of Fig. 1b and tracks 2 and 4 the lower layer. The total width of the GP was 10 cm with a gap of 4.4 cm. The lengths of the cuts ℓ_g were 3 mm and 5 cm.

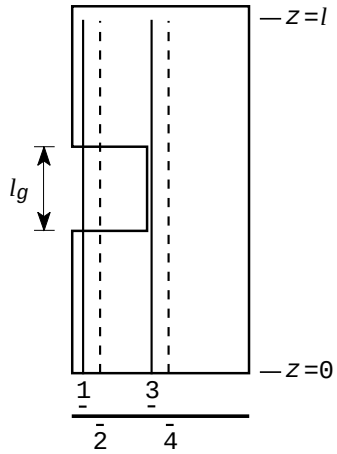

Fig. 27. A 10 cm wide ground plane with a cut of length ℓ_g. The tracks were $\ell = 20$ cm long, while the GP was 20.5 cm long. The upper solid lines corresponds to the upper layer of the PCB and the dashed lines to the lower layer.

Consider first the DM-CM coupling (or Bersier). The mutual inductance coefficients can

Table I. Calculated M_t and measured M_m mutual DM-CM inductances for the configuration of Fig. 27 in which at $h_{cp} = 1$ cm a CP was below the structure. Cuts of $\ell_g = 3$ mm and $\ell_g = 5$ cm were considered; M_{ng} denotes the mutual inductance assuming $\ell_g = 0$.

		$\ell_g = 3$ mm		$\ell_g = 5$ cm	
track	M_{ng} [nH]	M_t [nH]	M_m [nH]	M_t [nH]	M_m [nH]
1	1.0	1.4	5.8	7.7	14.0
2	3.0	3.3	7.3	9.0	15.0
3	0.3	0.3	0.5	1.1	1.4
4	2.9	3.0	4.0	3.4	4.7

be calculated with the method given in Appendix C5 of Report I. The inductive coupling from the DM track above the wide GP (10 cm) to the CM circuit is denoted by M_c (per unit length); the coupling from the DM track above the 'small' GP (5.6 cm) is denoted by M_g. In a very simple picture the total mutual inductance M_t of the DM track then equals

$$M_t = M_c(\ell - \ell_g) + M_g\ell_g \tag{18}$$

Table I shows the calculated and measured inductances M_t for ℓ_g 3 mm and 5 cm; for comparison the mutual inductance M_{ng} without a gap is also given.

Although the calculated coefficients are based on a 2D model, good correspondence between measurements and calculations are seen, certainly for $\ell_g = 5$ cm. The only significant deviation occurs for the upper track 1, this is because the effect of the vertices is neglected. For continuous GPs the coupling at the upper side is weaker than at the lower side. This effect also holds for our GP with gap. Therefore, the vertices have more influence for tracks at the upper side than at the lower side, certainly when such a track is routed above a gap (tracks 1 and 2). Of course, the vertices have less influence when the gap becomes longer, therefore the 5 cm calculations are in better agreement with measurements than the 3 mm calculations. For track 4 the calculations agree within 40 percent (3 dB) with the measurements. This track was approx. 1 cm from the gap, i.e. 7 times the height of the dielectric layer. For such positions the influence of the gap becomes less important.

As can be seen from table I, a gap in the GP increases the mutual coupling (and therefore also the capacitive coupling) which also depend significantly on the track position. A good advise is therefore never route a track over a gap, always strive towards a situation where such a track is sufficient far away from the gap, i.e., at least a few times the height of the dielectric layer. Note that this rule is in agreement with a remark [23, Sect. IX] from Report I: avoid tracks near edges.

The measured transfer impedances Z_T have the same behavior as for a GP without gap (see e.g. Fig. 12), the only difference is of course a larger coupling. Therefore, these curves are not given here. Certainly, Eq. (18) can be used to estimate the CM-current generation of tracks routed above a gap as long as resonances don't show up; see Sect. VIII of Report I. No attempts were made to calculate the transfer impedances or the quotient I_{CM}/I_{inj} in the Bersier setup with a TL model. The purpose of this experiment was to show the importance of a cut in a continuous GP.

The DM-DM crosstalk situation is much more complicated than the previous one. Since the coupling is more local, the effect of the vertices becomes a dominant factor. For example,

Table II. Measured M_m mutual DM-DM inductances for the configuration of Fig. 27 with $\ell_g = 3$ mm and $\ell_g = 5$ cm long cuts. For comparison the calculated inductances M_{ng} with $\ell_g = 0$ are given.

		$\ell_g = 3$ mm		$\ell_g = 5$ cm	
	M_{ng} [nH]	M_m [nH]	M_m/M_{ng}	M_m [nH]	M_m/M_{ng}
1 – 2	1.91	15.60	8.2	51.09	26.7
1 – 3	0.17	1.02	6.0	3.37	19.8
1 – 4	0.05	0.44	8.3	1.42	26.8
2 – 3	0.03	0.84	27.1	3.27	105.5
2 – 4	0.14	0.55	4.0	1.52	10.9
3 – 4	0.02	0.04	2.1	0.15	8.7

the measured mutual coupling coefficient of Z_T(1-2) was more then 20 dB higher than the calculated one (based on the same approach as the DM-CM case). A similar factor was found at low frequencies. The calculated mutual coefficient of Z_T(3-4) agreed with the measured one. For tracks sufficiently far away from the gap we can use the 2D and TL calculations. In order to calculate correctly the coupling for tracks routed above a gap, three-dimensional (3D) calculations are necessary. Such 3D calculations fall outside the scope of this report.

Table II shows the measured mutual inductance coefficients for our GP with gap and the calculated coefficients when no gap is present. As the results in the table show and one can intuitively feel: a track routed above a gap increases the crosstalk tremendously.

VIII. Concluding remarks

The proposed TL method estimates the equivalent sources for the common-mode current on a cable connected to a PCB quite well. Although for complicated tracks there is deviation between measurements and calculations above approx. 400-500 MHz, our TL method generally overestimates I_{CM}. Furthermore, for digital circuits the first few harmonics above 30 MHz, for which the current-injection or Bersier method is applicable, are dominant. Therefore, it is important to predict these dominant frequency components correctly.

One should realise the importance of the sharp resonances in the DM and CM circuits. Small errors in the calculated resonance frequency may be caused by parasitic elements of tracks and ICs. When the harmonics generated by digital circuits nearly coincide with a such resonance, large deviations may be found when compared to the measurements. This is true for our method, but also for the more complicated full-wave analysis.

The resonances are strongly damped when the DM tracks are terminated into their characteristic impedances. ECL-logic normally operates with characteristic termination. Sometimes a series resistor is mounted at the inputs of HLL logic, to provide correct termination at high frequencies. For the characteristic termination one may estimate the CM current by the method given in Sect. VIII of Report I, since then Z_T(DM-CM) is dominantly inductive (see Sect. III).

Of course, the method can be extended to higher frequencies when three-dimensional effects are more accurately included, e.g. fringing fields and capacitive couplings of the orthogonal tracks. These 3D additions to the model fall outside the scope of this study.

Appendix A [1]

Several approaches are possible for solving electromagnetic problems which involve perfectly conducting metallic structures and dielectrics. When only homogeneous dielectrics occur, the problem can be solved by means of equivalent sources; see Collin [46, Sect. 1.8] for a comprehensive overview. In this Appendix we will solve two-dimensional (2D) electrostatic problems. The small coupling capacitances involved are of main interest here. The analytical treatment and the numerical implementation are discussed in the first two subsections. Experiments show the importance of the discretization when the capacitances involved are small (of the order of fF/m), therefore the third subsection is devoted to the discretization. Finally, a comparison is made between the numerical solution with the analytical approximation (11) given in the main text.

1. Analytical treatment

Electrical potential problems for finite two-dimensional structures have been solved in the past by several authors, see e.g. Harrington *et al.* [47], and more recently Venkataraman *et al.* [48]. In this subsection a mathematical foundation for the resulting integral equations (IEs) over the conductor and dielectric-to-dielectric interfaces is given. In order to keep the derivation simple, i.e. avoiding a lot of bookkeeping, a simple structure is considered (see Fig. A1). An extension to more complex structures is readily made.

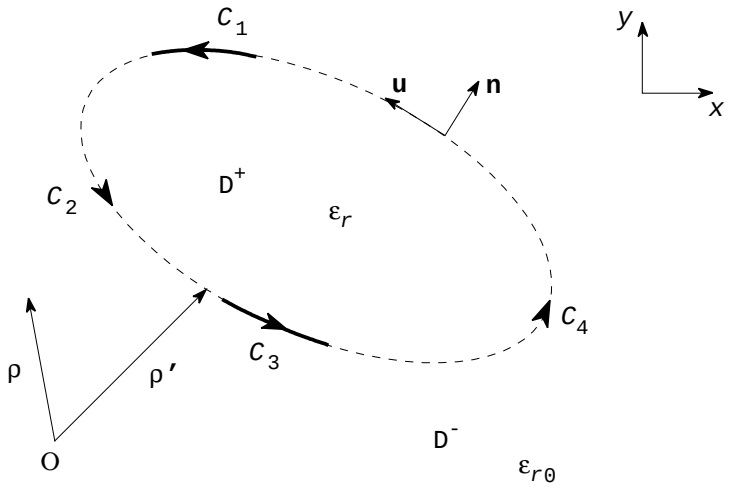

Fig. A1. Geometry of the problem.

Consider a two-dimensional dielectric body $\mathcal{D}^+$ with relative permittivity ε_r, which is bounded by a simple smooth closed contour $C = \cup C_k$ (see Fig. A1); C_1 and C_3 are infinitely thin ideal conductors and C_2 and C_4 dielectric boundaries. The unbounded outside region $\mathcal{D}^-$ consists of a dielectric with relative permittivity ε_{r0}, e.g. vacuum. For convenience denote the dielectric-dielectric interfaces by $C_d = C_2 \cup C_4$.

[1] The authors are indebted to prof. dr. J. Boersma from the Department of Mathematics and Computing science, for carefully reading this appendix and the useful suggestions made.

The unit vector $\mathbf{n}$ denotes the outward unit normal to C and C is travelled counterclockwise; the corresponding direction of the unit tangent $\mathbf{u}$ to C is shown in Fig. A1. The vector ρ denotes the position vector of the observation point $(x, y) \in I\!R^2$.

According to Harrington [47, Sect. 8.1], the potential at any point $\rho \in I\!R^2 \setminus C$ can be represented by

$$\Phi(\rho) = \int_C \frac{\sigma_T(\rho')}{2\pi\varepsilon_0} \ln \frac{K}{|\rho - \rho'|}\, \mathrm{d}s = \int_C \frac{\sigma_T(\rho')}{2\pi\varepsilon_0} \ln \frac{1}{|\rho - \rho'|}\, \mathrm{d}s + K' \int_C \frac{\sigma_T(\rho')}{2\pi\varepsilon_0}\, \mathrm{d}s, \tag{A1}$$

in which $\rho' \in C$, s is the arc length along C, σ_T is the total real-valued single-layer density and $K > 1$ is an arbitrary constant; therefore $K' = \ln K$ is also an arbitrary positive constant. Since $\Phi(\rho)$ is harmonic for $\rho \in I\!R^2 \setminus C$ and regular at infinity, the potential must be bounded for $|\rho| \to \infty$. This condition can only be satisfied when the total charge equals zero, i.e.

$$\int_C \sigma_T(\rho')\, \mathrm{d}s = 0. \tag{A2}$$

The potential (A1) of the single layer is continuous at all points on the curve C; see e.g. Tikhonov and Samarskii [49, Sect. IV.5]. Thus we are led to the integral equations

$$\int_C \frac{\sigma_T(\rho')}{2\pi\varepsilon_0} \ln \frac{K}{|\rho - \rho'|}\, \mathrm{d}s = V_1, \quad \rho \in C_1, \tag{A3}$$

$$\int_C \frac{\sigma_T(\rho')}{2\pi\varepsilon_0} \ln \frac{K}{|\rho - \rho'|}\, \mathrm{d}s = V_3, \quad \rho \in C_3, \tag{A4}$$

where V_1 and V_3 are the prescribed potentials at conductors C_1 and C_3, respectively.

The electric field $\mathbf{E}(\rho)$ is given by

$$\mathbf{E}(\rho) = -\nabla\Phi(\rho). \tag{A5}$$

The normal component of the electric flux density $\mathbf{D}$ must be continuous at the dielectric-dielectric interface C_d, therefore

$$\varepsilon_r \mathbf{n} \cdot \nabla\Phi(\rho^+) = \varepsilon_{r0} \mathbf{n} \cdot \nabla\Phi(\rho^-), \tag{A6}$$

where $\nabla\Phi(\rho^\pm) = \lim_{\delta \downarrow 0} \nabla\Phi(\rho \mp \delta\mathbf{n})$, and $\rho \in C_d$. Since $\mathbf{n} \cdot \nabla$ equals the normal derivative, the boundary condition (A6) for $\rho \in C_d$ yields [49, Sect. IV.5]

$$\varepsilon_r \left[\frac{\partial\Phi(\rho)}{\partial n} + \frac{\sigma_T(\rho)}{2\varepsilon_0} \right] = \varepsilon_{r0} \left[\frac{\partial\Phi(\rho)}{\partial n} - \frac{\sigma_T(\rho)}{2\varepsilon_0} \right], \quad \rho \in C_d, \tag{A7}$$

with

$$\frac{\partial\Phi(\rho)}{\partial n} = -\int_C \frac{\sigma_T(\rho')}{2\pi\varepsilon_0} \frac{d}{dn} \ln|\rho - \rho'|\, \mathrm{d}s = \int_C \frac{\sigma_T(\rho')}{2\pi\varepsilon_0} \frac{\cos\varphi}{|\rho - \rho'|}\, \mathrm{d}s, \quad \rho \in C_d, \tag{A8}$$

where φ is the angle between $\mathbf{n}$ and the direction from ρ to ρ'. Observe that the integral is proper since the integrand is continuous. The resulting integral equation for an observation point $\rho \in C_d$ becomes

$$\frac{\varepsilon_r + \varepsilon_{r0}}{2\varepsilon_0} \sigma_T(\rho) + \frac{\varepsilon_r - \varepsilon_{r0}}{2\pi\varepsilon_0} \int_C \sigma_T(\rho') \frac{\cos\varphi}{|\rho - \rho'|}\, \mathrm{d}s = 0, \quad \rho \in C_d. \tag{A9}$$

A frequently used method to solve the coupled IEs (A3), (A4), and (A9) is the method of moments (MOM), see Harrington [47, 50]. One of the simplest procedures expands σ_T in a series of pulse functions; see the next subsection. Point matching for testing yields a (non singular) matrix equation from which σ_T follows.

When the total single-layer density σ_T is known, the free-charge densities σ_F on the conductors are obtained by [48, Sect. III]

$$\sigma_F(\rho) = \frac{\varepsilon_r + \varepsilon_{r0}}{2}\sigma_T(\rho) + \frac{\varepsilon_r - \varepsilon_{r0}}{2\pi} \int\limits_C \sigma_T(\rho') \frac{\cos\varphi}{|\rho - \rho'|}\, \mathrm{d}s, \tag{A10}$$

with $\rho \in C_1$ and $\rho \in C_3$ for conductors C_1 and C_3, respectively.

Energizing conductor C_1 with potential $V_1 \neq 0$ and holding $V_3 = 0$ at conductor C_3, the capacitance C_{13} between the conductors equals the quotient $-Q_3/V_1$ with

$$Q_3 = \int\limits_{C_3} \sigma_F(\rho')\, \mathrm{d}s \tag{A11}$$

the total induced free-charge on conductor C_3. In this case Q_3 equals the total free-charge $-Q_1$ on conductor C_1.

2. Numerical implementation

The numerical implementation is done in complex arithmetic. Let $z = x + jy \in \mathbb{C}$ represent a point $(x, y) \in \mathbb{R}^2$ in space, and let $u = u_x + ju_y$ the complex representation of the unit tangent vector $\mathbf{u} = (u_x, u_y)$ along C. The electric field $\mathbf{E} = (E_x, E_y)$ is denoted by $E = E_x + jE_y$ in the complex domain.

Consider finite structures (as in Fig. A1) in which the boundary consists of straight lines. The structure consists of N_c conductors and N_d dielectric interfaces; $N_c = N_d = 2$ for the structure given in Fig. A1. The N_c conductors are subdivided into k straight-line segments and the N_d dielectric interfaces are subdivided into n straight-line segments. The set $Sc = \cup_{i=1}^{k} S_i$ contains the k conductor segments, whereas the set $Sd = \cup_{i=k+1}^{k_t} S_i$, $k_t = k + n$, contains the n dielectric segments. The total boundary then equals $S = Sc \cup Sd = \cup_{i=1}^{k_t} S_i$.

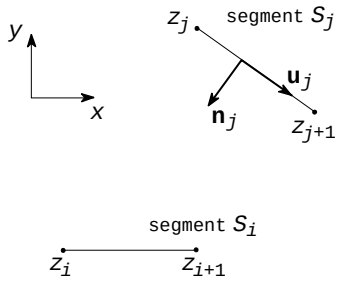

Fig. A2. Two line segments.

A segment S_j (see Fig. A2) with vertices $\{z_j, z_{j+1}\}$ has a length l_j. We approximate the actual single-layer density σ_T by a uniform single-layer density σ_{Tj} on S_j. Traveling from z_j to z_{j+1}, the relative permittivity is denoted by $\varepsilon_{rl,j}$ and $\varepsilon_{rr,j}$ as the left-hand and right-hand sides of S_j, respectively. The normal $\mathbf{n}_j$ points to the right-hand side of S_j (see Fig. A2), in accordance with Fig. A1.

The complex potential $\psi(z)$ at $z \in \mathbb{C}$ in 2D due to a line charge at $z' \neq z$ is given by $\psi(z) = -\log(z - z')/2\pi\varepsilon_0 + K_1$ (K_1 arbitrary positive). The potential $\psi_i(z)$ at z due to a constant single-layer density σ_{Ti} along a segment S_i with vertices $\{z_i, z_{i+1}\}$ (see Fig. A2) equals for $z \notin S_i$ [47, Sect. 3]

$$\begin{aligned}\psi_i(z) &= \frac{\sigma_{Ti}}{2\pi\varepsilon_0}\frac{1}{u_i}\int_{z_i}^{z_{i+1}} \log\frac{K_2}{z-z'}\mathrm{d}z' \\ &= \frac{\sigma_{Ti}}{2\pi\varepsilon_0}\left[\frac{z-z_i}{u_i}\log\frac{z-z_{i+1}}{z-z_i} + l_i\left(1+\log\frac{K_2}{z-z_{i+1}}\right)\right], \end{aligned} \tag{A12}$$

with $K_2 > 1$. This complex function is made single-valued by introducing a cut along S_i.

For the electric field E at $z \notin S_i$ we find

$$E(z)^* = E_x(z) - jE_y(z) = -\frac{d\psi_i(z)}{dz} = -\frac{\sigma_{Ti}}{2\pi\varepsilon_0}\frac{1}{u_i}\log\left(\frac{z-z_{i+1}}{z-z_i}\right), \tag{A13}$$

which is single-valued due to the cut along S_i. The normal component E_n of the electric field on a segment $S_j \neq S_i$, becomes (see [47, Sect. 3])

$$E_n(z) = -\mathrm{Re}\left[n_j\frac{d\psi_i(z)}{dz}\right] = -\mathrm{Im}\left[u_j\frac{d\psi_i(z)}{dz}\right], \quad z \in S_j, \quad i \neq j, \tag{A14}$$

with n_j and $u_j = jn_j$ the complex representations of the normal $\mathbf{n_j}$ and tangent $\mathbf{u_j}$ vectors on segment S_j, respectively. For $i = j$ we have,

$$E_n(z) = -\mathrm{Im}\left[u_j\frac{d\psi_j(z)}{dz}\right] = -\frac{\sigma_{Tj}}{2\pi\varepsilon_0}\mathrm{Im}\left[\log\left(\frac{z-z_{j+1}}{z-z_j}\right)\right] = \mp\frac{\sigma_{Tj}}{2\pi\varepsilon_0}, \quad z \in S_j \in S, \tag{A15}$$

in which the minus-sign is taken for the normal electric field at the left-hand side of S_j and the positive sign is taken for the right-hand side.

Let $E_{nt,j}$ denote the 'total' normal component of the electric field at segment S_j due to the single-layer density σ_{Ti} at segments S_i, with $i = 1, \cdots, k_t$, and $i \neq j$. By means of (A14) we have

$$E_{nt,j}(z) = -\sum_{\substack{i=1\\ i\neq j}}^{k_t}\mathrm{Im}\left[u_j\frac{d\psi_i(z)}{dz}\right], \quad z \in S_j \in S. \tag{A16}$$

The normal electric-field components at the left-hand and right-hand sides of S_j are denoted by $E_{nl,j}$ and $E_{nr,j}$, which become by means of (A15)

$$E_{nl,j}(z) = E_{nt,j}(z) - \frac{\sigma_{Tj}}{2\varepsilon_0} \quad \text{and} \quad E_{nr,j}(z) = E_{nt,j}(z) + \frac{\sigma_{Tj}}{2\varepsilon_0}, \tag{A17}$$

with $z \in S_j \in S$.

Since the conductors are imbedded in dielectrics, the conductor segment $S_j \in Sc$ is contained in dielectrics. The total single-layer density σ_{Tj} can be split into its free component σ_{Fj} and the bounded polarization component σ_{Bj}. The normal component of the dielectric flux density $\mathbf{D}$ is discontinuous over the conductor segment S_j and equals

$$\sigma_{Fj}(z) = D_{nr,r}(z) - D_{nl,r}(z) = \varepsilon_0\varepsilon_{rr,j}E_{nr,j}(z) - \varepsilon_0\varepsilon_{rl,j}E_{nl,j}(z), \quad z \in S_j \in Sc \tag{A18}$$

with $D_{nl,j}$ and $D_{nr,j}$ denoting the normal D-field components at the left-hand and right-hand sides of S_j, respectively. Observe that (A18) also holds at a dielectric-interface segment $S_j \in Sd$ because there $\sigma_{Fj} = 0$. Substitution of (A17) in (A18) yields

$$\sigma_{Fj}(z) = (\varepsilon_{rr,j} + \varepsilon_{rl,j})\frac{\sigma_{Tj}}{2} + (\varepsilon_{rr,j} - \varepsilon_{rl,j})\varepsilon_0 E_{nt,j}(z), \quad z \in S_j \in Sd. \tag{A19}$$

A matrix equation is obtained by using point matching; e.g. choose the midpoint $z = z_{mj} = (z_j + z_{j+1})/2$ at every segment S_j, $j = 1, \cdots, k_t$. The electrical potential should be constant on the conductors. Let the potentials on the N_c conductors be denoted by V_p, $p = 1, \cdots, N_c$. On the conductor segment S_j that is part of the conductor p, the potential is given by $V_{sj} = V_p$. The complex potential due to a constant single-layer density σ_{Ti} along the segment $S_i \in S$ is given by (A12). The real part of (A12) yields the electrical potential, which is continuous for $z \in S_i$. One obtains

$$\mathrm{Re}\left[\sum_{i=1}^{k_t} \psi_i(z_{mj})\right] = V_{sj}, \quad j = 1, \cdots, k. \tag{A20}$$

This may be shortly written as a matrix equation

$$\mathbf{\Psi}\sigma_{\mathbf{T}} = \mathbf{V_s}, \tag{A21}$$

with $\mathbf{\Psi}$ a $k \times k_t$ matrix, $\sigma_{\mathbf{T}} = (\sigma_{T1}, \cdots, \sigma_{Tk_t})^T$, and $\mathbf{V_s} = (V_{s1}, \cdots, V_{sk})^T$.

Almost the same procedure can be used for the dielectric-interface segments $S_i \in Sd$. One obtains by means of (A16), (A19), and $\sigma_{Fj} = 0$

$$(\varepsilon_{rr,j} + \varepsilon_{rl,j})\frac{\sigma_{Tj}}{2} + (\varepsilon_{rr,j} - \varepsilon_{rl,j})\varepsilon_0 E_{nt,j}(z_{mj}) = 0, \quad j = k+1, \cdots, k_t. \tag{A22}$$

This system may be shortly written as

$$\mathbf{\Psi_d}\sigma_{\mathbf{T}} = \mathbf{0}, \tag{A23}$$

with $\mathbf{\Psi_d}$ a $n \times k_t$ matrix representing (A22) and $\mathbf{0}$ the n-zero vector.

The total matrix equation becomes

$$\begin{bmatrix} \mathbf{\Psi} \\ \mathbf{\Psi_d} \end{bmatrix} \sigma_{\mathbf{T}} = \begin{bmatrix} \mathbf{V_s} \\ \mathbf{0} \end{bmatrix}, \tag{A24}$$

from which $\sigma_{\mathbf{T}}$ can be solved once the constant K_2 in (A12) is known. This constant vanishes when the first row of the matrix equation (A21) is subtracted from the other rows. Since the total charge must be zero, this condition is forced explicitly by replacing the k_t elements of the first row of matrix $\mathbf{\Psi}$ by l_i, $i = 1, \cdots, k_t$ and the first element of $\mathbf{V_s}$ is made zero; see [48]. Note that conductor p belonging to the first row is now at zero potential, therefore the potentials on the other conductors are relative to conductor p.

The free-charge density σ_F follows from (A19). The free charge on a conductor p is the sum of $\sigma_{Fi}l_i$ over the conductor segments S_i that belong to conductor p.

3. Discretization

The method is applied to the three layer PCB placed in vacuum (see Fig. A3). Our main interest is the small capacitive coupling C_{12} from track 1 to track 2; the self-capacitance C_1 is also given. The middle layer was a $2w = 10$ cm wide ground plane GP. The tracks of width $b = 1.5$ mm were located at a distance $h_1 = 1.5$ mm above and $h_2 = 1.5$ mm below the GP. The epoxy layer (- - - in Fig. A3) had a homogeneous dielectric permittivity $\varepsilon_r = 4.7$. The position of both tracks resulted in a minimum coupling capacitance.

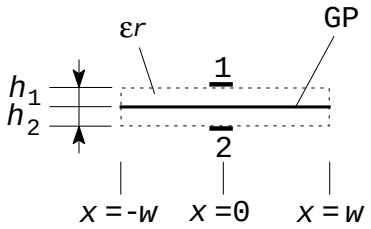

Fig. A3. Three layer PCB with an ideal ground plane (GP) of width $2w$. The ideal tracks of width b are located h_1 and h_2 above and below the GP, respectively.

We first consider the situation with the dielectric absent, i.e. only the conductors remain in vacuum. Later the dielectric is added.

No dielectric present

Without dielectric a first-order approximation of C_{12} is given by Kaden [51, Eq. (I.10)]

$$C_{12}^a = \frac{h_1 h_2 C_1 C_2}{4\pi\varepsilon_0 w^2}, \tag{A25}$$

in which C_1, C_2 are the self capacitances (see expression (3) in the main text with $\varepsilon_{r,eff} = 1$); for our situation $C_1 = C_2 = 26.8$ pF/m.

Numerically C_{12} and C_1 were obtained by applying a potential $V_1 = 1$ at track 1 with $V_2 = V_{GP} = 0$. The induced free-charges $Q_2(< 0)$ on track 2 and $Q_{GP}(< 0)$ on GP were obtained by means of the method discussed at the end of the previous subsection. Then $C_{12} = -Q_2/V_1$ and $C_1 = -Q_{GP}/V_1$.

Track 1, track 2, and the ground plane GP are divided into k_1, k_2, and k_3 segments; the total number of segments is denoted by $k_t = k_1 + k_2 + k_3$. In the homogeneous-discretization case all segments belonging to the same conductor have equal lengths. The lengths of these segments are not equal for the nonhomogeneous-discretization case, to be discussed below.

In Table AI the C_{12} and C_1 sequences are given for a homogeneous (h) discretization. The first-order analytical approximation (A25) leads to $C_{12}^a = 5.81$ fF/m. The numerical C_{12}-sequence seems to converge to the exact value when the number of segments are increased. Observe also that the numerically and analytically obtained self-capacitance C_1 agree within 3.5 percent.

Another approach is a nonhomogeneous (nh) discretization with the number of segments per conductor fixed. Since the tangential electric field E_{tan} of an ideal conductor is zero, the error η_j at segment S_j defined by

$$\eta_j = \sum_{i=1}^{k} \int_{S_j} |E_{tan,i}^j| \, |\mathrm{d}z|, \tag{A26}$$

Table AI. Coupling capacitance C_{12} and self-capacitance C_1 for the structure of Fig. A3 without dielectric: results for a homogeneous (h) and a nonhomogeneous (nh) discretization (see text). The number of segments used in track 1 (k_1), track 2 (k_2), and GP (k_3) is denoted by $(k_1, k_2, k_3; k_t)$, with $k_t = k_1 + k_2 + k_3$ the total number of segments.

	$(k_1, k_2, k_3; k_t)$				
	(10,10,50;70)	(20,20,100;140)	(20,20,200;240)	(20,20,400;440)	(20,20,800;840)
C_{12}(h) in fF/m	52.76	16.73	6.91	5.72	5.57
C_{12}(nh) in fF/m	5.46	5.58	5.59	5.63	5.63
C_1(h) in pF/m	25.87	26.14	26.17	26.17	26.17
C_1(nh) in pF/m	26.34	26.37	26.37	26.37	26.37

is a measure for the deviation of the calculated tangential-field compared with the physical 'zero-field'; $E^j_{tan,i}$ denotes the numerically calculated tangential field at S_j due to a single-layer density σ_{Fi} along a segment S_i.

In an iterative process the discretization is changed: the process starts with a homogeneous discretization. The next steps are: (1) The error η_j of segment S_j, $j = 1, \cdots, k_t$ is determined by calculating the potential at several additional points on each conductor segment. (2) The cumulative sum of η_j for the segments S_j belonging to the same conductor is determined. (3) This cumulative sum is used to redistribute the segments over the conductor where they belong to: a finer discretization where the sum changes fast. The total number of segments per conductor is kept constant. (4) The process iterates from step (1) until every segment S_j belonging to same conductor contributes the same error η_j and the total error per conductor converges to within a certain percentage; in the calculations 2 percent was used.

Table AI shows the calculated C_{12} and C_1 for this nonhomogeneous case; the total error of 2 percent per conductor was reached in 6 iterations. With relatively few segments (in this case 70) the coupling capacitance C_{12} can be accurately calculated. The numerically calculated self-capacitance C_1 agrees within 2 percent compared to the analytically obtained value of 26.8 pF/m.

Dielectric present

The dielectric boundaries (- - -, Fig. A3) and the conductors of the PCB structure are divided into k_t segments. Again, track 1, track 2, and ground plane GP are divided into k_1, k_2, and k_3 segments. The remaining $k = k_t - k_1 - k_2 - k_3$ segments are distributed proportional to the length of the eight straight dielectric interfaces. In the homogeneous-discretization case all segments belonging to the same dielectric-interface/conductor have equal lengths. The lengths of these segments varied for the nonhomogeneous-discretization case.

First results showed a large variation of the normal electric-field $\mathbf{E_n}$ along the dielectric-interfaces. Therefore, (A19) is integrated over a dielectric-interface segment $S_j \in Sd$. By means of

$$\int_{z_j}^{z_{j+1}} E_n \, |\mathrm{d}z| = -\mathrm{Im}\left[\psi_i(z_{j+1}) - \psi_i(z_j)\right], \tag{A27}$$

and $\sigma_{Fj} = 0$ we have

$$(\varepsilon_{rr,j} + \varepsilon_{rl,j})\frac{\sigma_{Tj}}{2} l_j - (\varepsilon_{rr,j} - \varepsilon_{rl,j})\varepsilon_0 \sum_{\substack{i=1 \\ i \neq j}}^{k_t} \mathrm{Im}\left[\psi_i(z_{j+1}) - \psi_i(z_j)\right] = 0, \quad j = k+1, \cdots, k_t. \quad \text{(A28)}$$

Eq. (A22) is replaced by (A28) from which the elements of the new matrix $\mathbf{\Psi_d}$ follow.

Numerically C_{12} was obtained by applying a potential $V_1 = 1$ at track 1 with $V_2 = V_{GP} = 0$. The free-charge $Q_1(> 0)$ on track 1 and induced free-charges $Q_2(< 0$, track 2) and $Q_{GP}(< 0$, ground plane) were obtained by means of the method discussed at the end of the previous subsection. Then $C_{12} = -Q_2/V_1$.

The self-capacitance C_1 showed a weak dependance on the discretization as in the case without dielectric (Table AI). The numerical values agreed within 1.5 percent compared to the analytical value of 88.9 pF/m (see expressions (3) and (4) in the main text). Therefore, the C_1-sequence is not given.

Table AII. Capacitance C_{12} for the structure of Fig. A3 with $\varepsilon_r = 4.7$; a homogeneous and nonhomogeneous discretization was used. The number of segments used in track 1 (k_1), track 2 (k_2), and ground plane GP (k_3) is denoted by $(k_1, k_2, k_3; k_t)$, with k_t the total number of segments. The ratio of the total free-charge Q and the induced free-charge Q_2 on conductor 2 is only calculated for the nonhomogeneous case.

	C_{12} in fF/m				
$(k_1, k_2, k_3; k_t)$	(20,20,100;400)	(20,20,200;700)	(20,20,300;1000)	(20,20,400;1250)	(20,20,640;2000)
homogeneous	59.01	9.78	4.75	3.53	2.85
nonhomogeneous	2.76	2.70	2.69	2.69	2.68
Q/Q_2	15.1	4.4	2.1	1.4	0.7

In Table AII the C_{12}-sequence is given for a homogeneous discretization. The sequence converges very slowly. On physical grounds the total free-charge must be zero for this isolated system, but the numerically calculated free charge $Q = Q_1 + Q_2 + Q_{GP} < 0$ is larger than the machine precision; without dielectric Q was smaller than the machine precision. Also, the numerical value of Q is of the same order as the induced free-charge Q_2 on conductor 2, which is used to obtain C_{12}. Since the convergence of C_{12} in Table AII is slow and Q is of the same order as Q_2, we changed the discretization.

On a dielectric-interface segment $S_j \in Sd$ the normal dielectric-flux density $D^j_{n,i}$ due to another segment S_i must be continuous. The error ζ_j defined by

$$\zeta_j = \frac{1}{\varepsilon_0} \left| (\varepsilon_{rr,j} + \varepsilon_{rl,j})\frac{\sigma_{Tj}}{2} l_j + (\varepsilon_{rr,j} - \varepsilon_{rl,j})\varepsilon_0 \sum_{\substack{i=1 \\ i \neq j}}^{k_t} \int_{S_j} |E^j_{n,i}(z)|\,|\mathrm{d}z| \right|, \quad \text{(A29)}$$

is a measure for the mismatch of the normal dielectric-flux density along segment $S_j \in Sd$; $E^j_{n,i}$ denotes the normal electric-field calculated by (A14) at the dielectric-interface segment S_j due to a single-layer density along segment S_i.

The iteration procedure for the PCB problem without dielectric can be used, in which besides the error η_j over the conductor segments also the error ζ_j over the dielectric-interface

segments must be used. Table AII shows C_{12} for several segments used; the procedure converged within 6 iterations. The ratio Q/Q_2 (see Table AII) decreases and becomes less than 1 for $k_t \approx$ 2000 segments. From this ratio sequence and the C_{12}-sequence one can conclude that the error is not made in Q_2. If the error was made in Q_2, then $Q/Q_2 \geq 1$. Experiments showed that the largest error made is due to the insufficient approximation of the $1/(x^2 + h_1^2)$ behavior of the charge density in the ground plane GP, rather than the edge divergence. Therefore, C_{12} converges to the exact value. Note that approx. $k_t = 400$ segments suffice for practical accuracy.

To get a reasonably accurate value of C_{12}, the total number of segments, k_t, must be impractically large for a homogeneous discretization. The nonhomogeneous case needs much less segments. Therefore, the memory requirement is much less demanding for the latter case: 2000 segments stored in double precision use approximately 30 MB, whereas 400 segments need only approximately 1 MB. The nonhomogeneous-discretization algorithm can also be used on 'simple' computers such as a PC. The process saves memory of the computer, rather then CPU time.

The numerical values clearly show the importance of the discretization on the small coupling capacitance. When both tracks are on the same side the capacitive coupling is of the order pF/m. Also, when the cabinet panel (CP) is present (see Fig. 7 main text), the capacitive coupling from a track to CP is again of the order pF/m. Numerical experiments showed that for such 'large' values a homogeneous discretization is allowed.

4. Numerical and approximate-analytical solution

Consider the PCB structure shown in Fig. A3. The parameters used were again $2w = 10$ cm, $b = 1.5$ mm, $h_1 = h_2 = 1.5$ mm, and $\varepsilon_r = 4.7$.

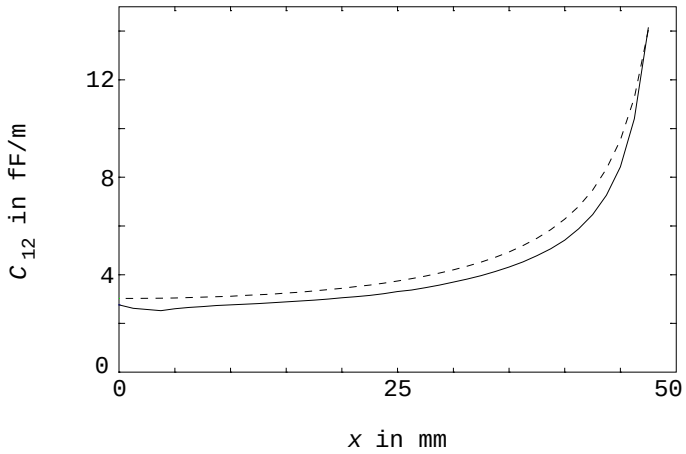

Fig. A4. Numerically (—) calculated coupling-capacitance $C_{12}(x)$ of track 1 to track 2 in Fig. A3. Track 1 was fixed at $x = 0$ while the positioning of track 2 was varied. Curve (- - -) shows the analytical approximation (11) given in the main text.

Figure A4 shows the numerically calculated $C_{12}(x)$ with track 1 fixed at $x = 0$ and the positioning of track 2 varied. In this configuration the capacitance involved has the lowest value. The analytical approximation (11) given in the main text is shown by curve (- - -). Both agree within 20 percent.

Appendix B

1. Common-mode radiation

The ground plane GP (Fig. B1) of width $2w$, length ℓ, and thickness d is at the $z = 0$ side connected with an infinite perfectly conducting plane. By image theory, the structure is equivalent to a GP of length 2ℓ. The spherical coordinates ϕ and θ are used, where ϕ is measured counterclockwise from the positive x axis and the polar angle θ is measured from the positive z axis.

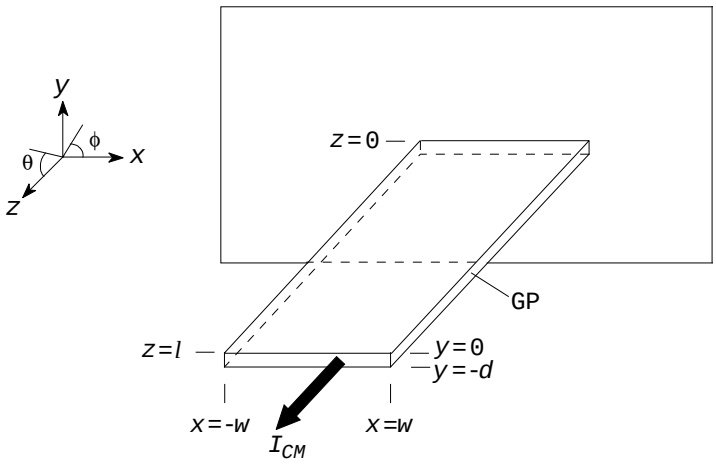

Fig. B1. Perspective view of the ground plane GP with dimensions $2w$, ℓ and d.

Assume that a common-mode current I_{CM} flowing in the GP returns very far away from structure, i.e. at infinity. The sheet-current density $K_z(x)$ then becomes

$$K_z(x) = \frac{I_{CM}}{\pi} \frac{1}{\sqrt{w^2 - x^2}}. \tag{B1}$$

Further, assume a sinusoidal variation in the z-direction. The current density $\mathbf{J}(x, y, z)$ then becomes

$$\mathbf{J}(x, y, z) = \frac{K_z(x)}{d} \sin\left(k_0[\ell - |z|]\right) \mathbf{e_z}, \tag{B2}$$

with $\mathbf{e_z}$ the unit vector pointing in the z-direction and k_0 the free-space propagation constant; the absolute sign around z is due to the image term.

The radiation vector $\mathbf{N}$ defined in Ramo *et al.* [25, Sect. 12.4], has only a non-trivial z-component

$$N_z = \int_{-\ell}^{\ell} \mathrm{d}z' \int_{-d}^{0} \mathrm{d}y' \int_{-w}^{w} \mathrm{d}x' \mathbf{J}(x', y', z') \cdot \mathbf{e_z} \mathrm{e}^{jk_0 \mathbf{o}\cdot\mathbf{r}'}, \tag{B3}$$

in which $\mathbf{o} \cdot \mathbf{r}' = x' \sin\theta\cos\phi + y' \sin\theta \sin\phi + z' \cos\theta$.

The integral over x involves special functions [52, Eq. (3.753.2)]

$$\int_{-w}^{w} K_z(x') \mathrm{e}^{jk_0 x' \sin\theta\cos\phi} \, \mathrm{d}x' \quad = \quad \frac{I_{CM}}{\pi} \int_{-1}^{1} \frac{\exp(jk_0 wp \sin\theta\cos\phi)}{\sqrt{1-p^2}} \, \mathrm{d}p$$

$$
\begin{aligned}
&= \frac{2I_{CM}}{\pi} \int_0^1 \frac{\cos(k_0 wp \sin\theta\cos\phi)}{\sqrt{1-p^2}}\,\mathrm{d}p \\
&= I_{CM} J_0(k_0 w \sin\theta\cos\phi),
\end{aligned}
$$

where $J_0(\cdot)$ is the zeroth-order Bessel function of the first kind. The integrals over y and z are elementary and are only given here for convenience

$$
\int_{-d}^{0} \mathrm{e}^{jk_0 y' \sin\theta\sin\phi}\,\mathrm{d}y' = 2\frac{\sin(k_0\frac{d}{2}\sin\theta\sin\phi)}{k_0\sin\theta\sin\phi}\mathrm{e}^{-j\sin\theta\sin\phi k_0 d/2} \approx d,
$$

and

$$
\int_{-\ell}^{\ell} \sin\left(k_0[\ell - |z'|]\right)\mathrm{e}^{jk_0 z'\cos\theta}\,\mathrm{d}z' = 2\frac{\cos(k_0\ell\cos\theta) - \cos(k_0\ell)}{k_0\sin^2\theta}.
$$

The approximation over y is valid for $k_0 d \ll 1$, which is certainly the case for our thin GP.

The radiation vector component N_z now becomes

$$
N_z = 2I_{CM}\frac{\cos(k_0\ell\cos\theta) - \cos(k_0\ell)}{k_0\sin^2\theta} J_0(k_0 w\sin\theta\cos\phi). \tag{B4}
$$

The average power radiated is [25, Sect. 12.4]

$$
P_{rad} = \frac{\eta_0}{8\lambda^2}\int_0^{2\pi}\mathrm{d}\phi\int_0^{\pi}\sin\theta\,\mathrm{d}\theta|N_z\sin\theta|^2, \tag{B5}
$$

in which η_0 is the free-space impedance and λ the wavelength. Since the original problem (Fig. B1) only considers the half space $z > 0$, this radiated power must be divided by a factor 2.

Finally, the radiation resistance is defined by

$$
R_{rad} = \frac{2P_{rad}/2}{|I_i|^2}, \tag{B6}
$$

with I_i the injection current at $z = 0$; the extra factor 2 as explained above.

2. Differential-mode radiation

The structure for DM case is shown in Fig. B2 for which the infinite plane has been removed. The source consists of a voltage generator V_g with impedance Z_g. For convenience $Z_g = Z_0$, the characteristic impedance of the TL formed by the track and GP. The current through the track is denoted by I_{DM} and has a amplitude I_1.

The current density $\mathbf{J_t}$ through the track (assuming the current concentrated at the middle of the track) is given by

$$
\mathbf{J_t} = I_1\delta(x - x_1)\delta(y - h_1)\left(\mathrm{e}^{j\beta(\ell - z)} + \rho_i\mathrm{e}^{-j\beta(\ell-z)}\right)\mathbf{e_z}, \tag{B7}
$$

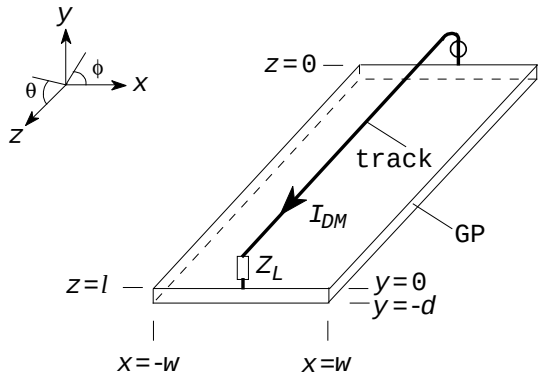

Fig. B2. Track at position (x_1, h_1) terminated via a load impedance Z_L with GP of dimensions $2w$, ℓ and d.

and the current density through GP by

$$\mathbf{J_{GP}}(x,y,z) = \frac{K_z(x)}{d}\left(\mathrm{e}^{j\beta(\ell-z)} + \rho_i \mathrm{e}^{-j\beta(\ell-z)}\right)\mathbf{e_z}, \tag{B8}$$

with $\delta(\cdot)$ Dirac's delta function, $K_z(x)$ the numerically calculated sheet-current density, $\rho_i = -(Z_L - Z_0)/(Z_L + Z_0)$ the current-reflection coefficient at $z = \ell$, and $\beta = \sqrt{\varepsilon_{r,eff}}k_0$ the effective propagation velocity of the wave. The current densities through the source and load are given by

$$\mathbf{J_v}(x,y,z) = I_1\delta(x-x_1)\left[H(y-h_1) - H(y)\right]\delta(z)\mathbf{e_y}, \tag{B9}$$

and

$$\mathbf{J_v}(x,y,z) = -I_1(1+\rho_i)\delta(x-x_1)\left[H(y-h_1) - H(y)\right]\delta(z-\ell)\mathbf{e_y}, \tag{B10}$$

in which $H(\cdot)$ denotes Heaviside's function. According to Lewin [53] the polarization-current density $\mathbf{J_p}$ can be approximated by

$$\mathbf{J_p}(x,y,z) = \frac{\varepsilon_{r,eff}-1}{\varepsilon_{r,eff}} 2h_1 \frac{\partial I_{DM}}{\partial z}\delta(x-x_1)\delta(y-h_1)\left[H(z-\ell) - H(z)\right]\mathbf{e_y}. \tag{B11}$$

The radiation vector $\mathbf{N}$ has now non-trivial y and z components

$$N_y = \int_0^{\ell}\mathrm{d}z' \int_{-d}^{0}\mathrm{d}y' \int_{-w}^{w}\mathrm{d}x' \mathbf{J}(x',y',z')\cdot\mathbf{e_y}\mathrm{e}^{jk_0\mathbf{o}\cdot\mathbf{r}'}, \tag{B12}$$

and

$$N_z = \int_0^{\ell}\mathrm{d}z' \int_{-d}^{0}\mathrm{d}y' \int_{-w}^{w}\mathrm{d}x' \mathbf{J}(x',y',z')\cdot\mathbf{e_z}\mathrm{e}^{jk_0\mathbf{o}\cdot\mathbf{r}'}, \tag{B13}$$

with $\mathbf{J}$ replaced by the above given current densities (B7)-(B11). Almost all integrals can be analytically calculated, except the x-dependant part of N_z for $\mathbf{J} = \mathbf{J_{GP}}$, which must be numerically integrated due to $K_z(x)$.

The radiated power now becomes

$$P_{rad} = \frac{\eta_0}{8\lambda^2}\int_0^{2\pi}\mathrm{d}\phi \int_0^{\pi}\sin\theta\,\mathrm{d}\theta\left[|N_\phi|^2 + |N_\theta|^2\right], \tag{B14}$$

in which $N_\phi = N_y \cos\phi$ and $N_\theta = N_y \sin\phi\cos\theta - N_z \sin\theta$. The radiation resistance equals

$$R_{rad} = \frac{2P_{rad}}{|I_i|^2}, \tag{B15}$$

with I_i the injection current at $z = 0$.

Figure B3 shows the radiation resistance calculated by this theory (no dielectric present) and by NEC[2] [54]; the parameters used were $Z_L = 0\ \Omega$, $Z_0 = 170\ \Omega$, $2w = 5$ cm, $h_1 = 5$ mm and $\ell = 0.2$ m. In NEC the GP was modeled by 1 mm thick wires; the structure has been created by means of the computer program Wiregrid[3] [55].

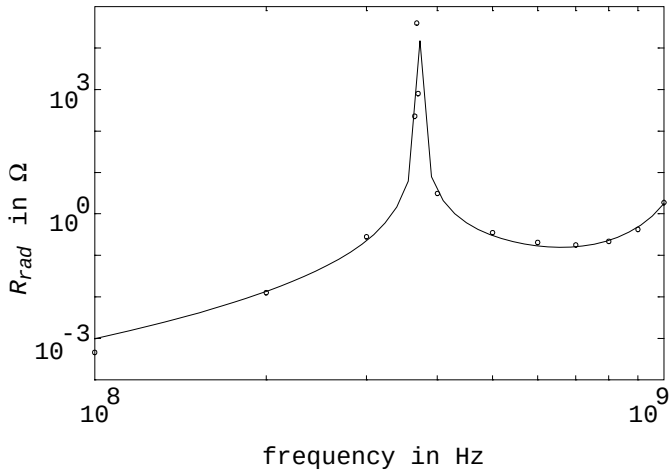

Fig. B3. Radiation resistance for the shorted structure given in Fig. B2 calculated by this theory (—) and NEC (o).

Good agreement between our theory and NEC is obtained. The main deviation at the resonance peak (NEC $f = 368$ MHz) is due to the input current I_i which becomes very small. The radiated power was the same within 6 dB.

[2]NEC2 source codes and executables for different computer platforms are distributed by the Applied Computational Electromagnetics Society (ACES) on Internet via the URL `ftp://emclab.ee.umr.edu/pub/aces/NEC`.

[3]A PC executable (`wiregrid.zip`) version is available via the above mentioned URL.

Appendix C

Consider the ground plane GP (Fig. C1) of width $2w$, length ℓ, and thickness d.

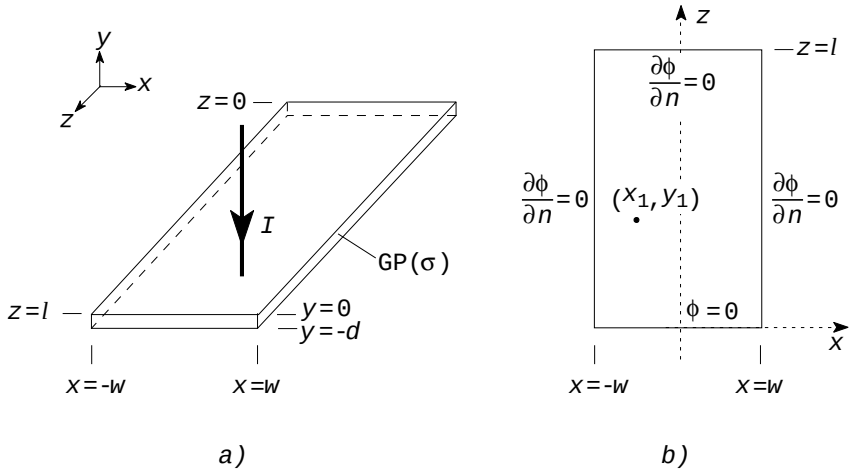

Fig. C1. a) Perspective view of the ground plane GP with dimensions $2w$, ℓ, and d. The thin wire with d.c. current I has coordinates (x_1, y_1, z), $y > 0$. b) Top view of the GP; the electrostatic potential ϕ is defined in the main text. The boundary conditions are as indicated, where n is the normal on the boundary which points outside the region.

A d.c. current I is injected through a very thin wire with coordinates (x_1, y, z_1), $y > 0$, which terminates perpendicular on the GP (see Fig. C1a). The current returns through the GP and leaves at the $z = 0$ end of Fig. C1. According to Van Bladel [39, Sect. 5.1] the current distribution $\mathbf{J}(x, y, z)$ equals the relation

$$\mathbf{J}(x, y, z) = -\sigma \nabla \tilde{\phi}(x, y, z), \tag{C1}$$

where $\tilde{\phi}(x, y, z)$ is the electrostatic potential in the GP. When the y dependence of $\mathbf{J}(x, y, z)$ is neglected, we get a two dimensional (2D) problem as indicated in Fig. C1b; the potential becomes $\phi(x, z) = \tilde{\phi}(x, y, z)$. The normal n points outside the region. On three sides of the boundary $\partial\phi(x, z)/\partial n$ is zero since the normal component of the current must be zero. On physical grounds, all the current must return perpendicular through the $z = 0$ side, therefore $\phi(x, 0)$ =const., for convenience choose this constant zero. By [39, Sect. 5.5]

$$\nabla^2 \phi(x, z) = -\frac{I}{\sigma d} \delta(x - x_1)\delta(z - z_1), \tag{C2}$$

with $\delta(\cdot)$ Dirac's delta function. Expanding the x direction in a Fourier cosine series, a solution of (C2) is

$$\phi(x, z) = A_0(z) + \sum_{k=1}^{\infty} A_k(z) \cos p(x + w), \tag{C3}$$

with $p = k\pi/2w$ (in the following it is assumed that k is a positive integer when only separate terms of the summation are used). This solution satisfies the boundary conditions $-\partial\phi/\partial x(-w, z) = 0$ and $\partial\phi/\partial x(w, z) = 0$. Partial differentiation of Eq. (C3) yields (see also [39, Sect. 1.11])

$$\nabla^2 \phi(x, z) = \ddot{A}_0(z) + \sum_{k=1}^{\infty} \left(\ddot{A}_k(z) - p^2 A_k(z) \right) \cos p(x + w), \tag{C4}$$

where $\dot{}$ denote the (ordinary) differentiation w.r.t. z. Expansion of $\delta(x-x_1)\delta(z-z_1)$ in a Fourier cosine series gives

$$\delta(x-x_1)\delta(z-z_1) = B_0(z) + \sum_{k=1}^{\infty} B_k(z)\cos p(x+w), \tag{C5}$$

from which

$$B_0(z) = \frac{1}{2w}\delta(z-z_1), \quad \text{and} \quad B_k(z) = \frac{\cos p(x_1+w)}{w}\delta(z-z_1). \tag{C6}$$

Substitution of (C4) and (C5) in Eq. (C2) and comparing the coefficients yields

$$\ddot{A}_0(z) = -\frac{I}{2\sigma w d}\delta(z-z_1) \tag{C7}$$

$$\ddot{A}_k(z) - p^2 A_k(z) = -Q_k\delta(z-z_1), \tag{C8}$$

with $Q_k = I/(\sigma w d)\cos p(x_1+w)$. The conditions $[A_0(0)=0,\ A_k(0)=0]$ and $[\dot{A}_0(\ell)=0,\ \dot{A}_k(\ell)=0]$ follow from the boundary conditions $-\partial\phi/\partial z(x,\ell)=0$ and $\phi(x,0)=0$, respectively. Eq. (C7) then becomes

$$\begin{aligned} \ddot{A}_0(z) &= -\frac{I}{2\sigma w d}\delta(z-z_1), \\ A_0(0) &= 0, \\ \dot{A}_0(\ell) &= 0, \end{aligned}$$

with solution (by twice integration)

$$A_0(z) = \begin{cases} \frac{I}{2\sigma w d} z & , \quad 0 < z < z_1 \\ \\ \frac{I}{2\sigma w d} z_1 & , \quad z_1 < z < \ell. \end{cases} \tag{C9}$$

The solution of Eq. (C8) with conditions $A_k(0)=0$ and $\dot{A}_k(\ell)=0$ can be found by standard techniques (see e.g. Dettman [56, Sects. 5.1 and 5.2]), and equals

$$A_k(z) = \begin{cases} C_k \sinh p(\ell-z) + D_k \cosh p(\ell-z) & , \quad 0 < z < z_1 \\ \\ E_k \cosh p(\ell-z) & , \quad z_1 < z < \ell, \end{cases} \tag{C10}$$

in which

$$\begin{aligned} C_k &= -\frac{Q_k}{p}\cosh p(\ell-z_1), \\ D_k &= \frac{Q_k}{p}\left(\cosh p(\ell-z_1) - \mathrm{e}^{-p\ell}\frac{\cosh p(\ell-z_1)}{\cosh p\ell}\right), \\ E_k &= \frac{Q_k}{p}\left(\mathrm{e}^{-p(\ell-z_1)} - \mathrm{e}^{-p\ell}\frac{\cosh p(\ell-z_1)}{\cosh p\ell}\right). \end{aligned}$$

For convenience, Fig. 2 from Report I is given in Fig. C2 with a slight modification. The sensing wire at the opposite side of the GP (i.e. $y<-d$) has coordinates $(x_2,-d,z_2)$ for point a. The induced voltage V_{DM} then becomes

$$V_{DM} = \int_{z_2}^{0} E_z \,\mathrm{d}z = -\int_{z_2}^{0} \frac{\partial\tilde{\phi}(x_2,-d,z)}{\partial z}\,\mathrm{d}z = \tilde{\phi}(x_2,-d,z_2) = \phi(x_2,z_2). \tag{C11}$$

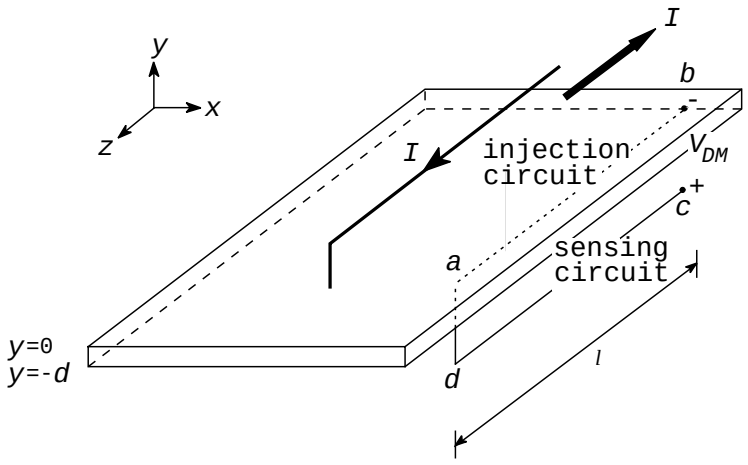

Fig. C2. The voltage V_{DM} measured between c and b is determined by the E_z-field along the line a-b and the flux through the area a-b-c-d-a.

With the above expressions, the transfer impedance $Z_T = V_{DM}/I$ yields for $0 < z_2 < z_1$

$$Z_T = \frac{R_\square}{2w} z_2 + \frac{2R_\square}{\pi} \sum_{k=1}^{\infty} \frac{1}{k} \frac{\sinh pz_2}{\cosh p\ell} \cosh p(\ell - z_1) \cos p(x_1 + w) \cos p(x_2 + w). \tag{C12}$$

with $p = k\pi/2w$, $R_\square = 1/\sigma d$. For $z_1 < z_2 < \ell$

$$Z_T = \frac{R_\square}{2w} z_1 + \frac{2R_\square}{\pi} \sum_{k=1}^{\infty} \frac{1}{k} \frac{\sinh pz_1}{\cosh p\ell} \cosh p(\ell - z_2) \cos p(x_1 + w) \cos p(x_2 + w), \tag{C13}$$

When x_1 and x_2 are approximately equal to 0 and $z_1 \uparrow \ell$, Z_T is approximated by

$$Z_T \simeq \frac{R_\square}{2w} z_2 - \frac{R_\square}{\pi} \ln\left(1 - \mathrm{e}^{-\pi(\ell - z_2)/w}\right). \tag{C14}$$

In the limit $z_2 \uparrow \ell$ one gets

$$Z_T \simeq \frac{R_\square}{2w} \ell - \frac{R_\square}{\pi} \ln \frac{\pi(\ell - z_2)}{w}. \tag{C15}$$

For the injection wire at position $(0, \ell/2)$, i.e. at the middle of the plane, and point a (Fig. C2) resides near this point ($x_2 \approx 0$ and $z_2 \approx \ell/2$), then

$$Z_T \simeq \frac{R_\square}{2w} \frac{\ell}{2} - \frac{R_\square}{\pi} \ln\left(1 - \mathrm{e}^{-\pi r/w}\right) \simeq \frac{R_\square}{2w} \frac{\ell}{2} - \frac{R_\square}{\pi} \ln \frac{\pi r}{w}, \tag{C16}$$

with r the radius of the sensing wire. From (C15) and (C16) we get the familiar $\ln 1/r$ behavior.

Figure C3 shows the percentage increase of the d.c. part of Z_T for a 5 cm wide plane compared with a homogeneous current distribution, i.e. $Z_T = \ell R_\square/2w$, with $R_\square = 1/\sigma d$ the sheet resistance of the GP. The injection wire terminates precisely on the edge ($z_1 = \ell$) and both wires resides near the middle of the GP ($x_{1,2} \approx 0$).

When the sensing wire is approx. 15 mm from the edge only 1 percent increase is obtained and can therefore be neglected. A considerable effect is obtained when the sensing wire is very

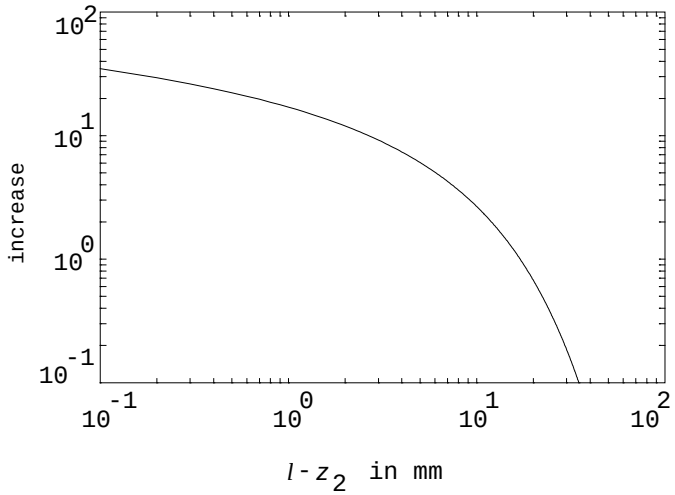

Fig. C3. Increase of the d.c. Z_T-resistance with point injection compared to situation where brass plate B exists (homogeneous case). The injection wire 1 terminates precisely on the edge, i.e. $z_1 = 0$ in Fig. 1, whereas the positioning of sensing wire 2 moves away from the edge. Both wires resides near the middle of the $2w = 5$ cm wide GP (i.e. $x_{1,2} \approx 0$ in Fig. 1b).

near the injection wire and both wires reside near the edge. Since the increase is logarithmic (see Eq.(C15)), it is to a certain extent bounded for realistic dimensions of the sensing wire.

Measurements obtained an increase of 60 percent for the setup of Fig. 1 without brass plate B; the current was injected in track 1 and the induced voltage V_{DM} was measured at track 2 and both wires were at the edge ($z_1 = z_2 = \ell$). The increment from 1 to 4 was negligible.

On the basis of Fig. C3, the 60 percent increase is probably not the only result of the point-injection effect. The local soldering of the injection wire also has a influence on the potential due to the lower conductivity of the solder. Therefore, the measured Z_T will be higher than the theoretical predicted one. Nevertheless, when the measuring wire is sufficient far away from the injection wire, the effect can be neglected.

References

[1] Abraham, M.
Funkentelegraphie und Elektrodynamik.
Phys. Zeitschrift, Vol. 2 (1901), No. 22, p. 329-334.

[2] Carson, J. R.
Radiation from transmission lines.
J. Am. Inst. Elec. Eng., Vol. 40 (1921), No. 10, p. 789-790.

[3] Manneback, C.
Radiation from transmission lines.
J. Am. Inst. Elec. Eng., Vol. 42 (1923), No. 2, p. 95-105.

[4] Kami, Y. and R. Sato
Analysis of radiation characteristics of a finite-length transmission line using a circuit-concept approach.
IEEE Trans. Electromagn. Compat., Vol. EMC-30 (1988), No. 2, p. 114-121.

[5] Nakamura, T. and K. Oda, S. Yokokawa
Equivalent transmission lines of wire antennas and the radiation mechanism.
Electron. Commun. Jpn. 1, Vol. 72 (1989), No. 8, p. 85-94.

[6] Green, H.E. and J. D. Cashman
The transmission line antenna revisited.
IEEE Trans. Antennas Propagat., Vol. AP-38 (1990), No. 4, p. 575-578.

[7] Nakkamura, T. and N. Hayashi, H. Fukuda, S. Yokokawa
Radiation from the transmission line with an acute bend.
IEEE Trans. Electromagn. Compat., Vol. EMC-37 (1995), No. 3, p. 317-325.

[8] Hill, D.A. and D.G. Camell, K.H. Cavcey, G.H. Koepke
Radiated emissions and immunity of microstrip transmission lines: Theory and reverberation.
IEEE Trans. Electromagn. Compat., Vol. EMC-38 (1996), No. 2, p. 165-172.

[9] Ott, H.W.
Controlling EMI by printed wiring board layout.
In: Proc. Electromagnetic compatibility 1985, 6th International Zurich symposium and technical exhibition on electromagnetic compatibility. Zürich, 5-7 March 1985. Ed. by T. Dvořák. Zürich: ETH Zentrum, 1985. P. 127-132.

[10] Paul, C.R. and D.R. Bush
Radiated emissions from common-mode currents.
In: Proc. IEEE 1987 International symposium on electromagnetic compatibility. Atlanta, GA, 14-17 August 1987. Piscataway, NJ: IEEE, 1987. P. 197-203.

[11] Paul, C.R.
A comparison of the contributions of common-mode and differential-mode currents in radiated emissions.
IEEE Trans. Electromagn. Compat., Vol. EMC-31 (1989), No. 2, p. 189-93.

[12] German, R.F. and H.W. Ott, C.R. Paul
Effect of an image plane on printed circuit board radiation.
In: Proc. IEEE 1990 International symposium on electromagnetic compatibility. Washington, DC, 21-23 August 1990. Piscataway, NJ: IEEE, 1990. P. 284-291.

[13] Dockey, R.W. and R.F. German
New techniques for reducing printed circuit board common-mode radiation.
In: Proc. IEEE 1993 International symposium on electromagnetic compatibility. Dallas, TX, 9-13 August 1993. Piscataway, NJ: IEEE, 1993. P. 334-339.

[14] Öing, S. and W. John, F. Sabath
Computation of common mode radiation due to asymmetric coupling on printed circuit boards.
In: Electromagnetic compatibility 1994, Twelfth international Wroclaw symposium and exhibition on electromagnetic compatibility. Wroclaw, 28 June-1 July 1994. Ed. by J.M. Janiszewski and W. Moron, W. Sega. Wroclaw: EMC symposium, 1994. P. 554-558.

[15] Drewniak, J.L. and T.H. Hubing, T.P. Van Doren
Investigation of fundamental mechanisms of common-mode radiation from printed circuit boards with attached cables.
In: Proc. IEEE 1994 International symposium on electromagnetic compatibility. Chicago, IL, 22-26 August 1994. Piscataway, NJ: IEEE, 1994. P. 110-115.

[16] Drewniak, J.L. and F. Sha, T.P. Van Doren, T.H. Hubing, J. Shaw
Diagnosing and modeling common-mode radiation from printed circuit boards with attached cables.
In: Proc. IEEE 1995 International symposium on electromagnetic compatibility. Atlanta, GA, 14-18 August 1995. Piscataway, NJ: IEEE, 1995. P. 465-470.

[17] Leroux, E. and S. Caniggia, F. Canavero, B. Demoulin
Evaluation of radiated emissions from printed circuit boards and cables at post-layout level.
In: Proc. EMC'96 Roma, International symposium on electromagnetic compatibility. Rome, 17-20 September 1996. Rome: EMC'96 Roma Secretariat, 1996. Vol. 2, p. 662-667.

[18] Hockanson, D.M. and C.-W. Lam, J.L. Drewniak, T.H. Hubing, T.P. Van Doren
Experimental and numerical investigation of fundamental radiation mechanisms in PCB designs with attached cables.
In: Proc. IEEE 1996 International symposium on electromagnetic compatibility. Santa Clara, CA, 19-23 August 1996. Piscataway, NJ: IEEE, 1996. P. 305-310.

[19] Hockanson, D.M. and J.L. Drewniak, T.H. Hubing, T.P. Van Doren, F. Sha, M.J. Wilhelm
Investigation of fundamental EMI source mechanisms driving common-mode radiation from printed circuit boards with attached cables.
IEEE Trans. Electromagn. Compat., Vol. EMC-38 (1996), No. 4, p. 557-566.

[20] Bersier, R. and B. Szentkuti
Rationale and new experimental evidence on the adequacy of conducted instead of radiated susceptibility tests.
In: Proc. Electromagnetic compatibility 1983, 5th International Zurich symposium and technical exhibition on electromagnetic compatibility. Zürich, 8-10 March 1983. Ed. by T. Dvořák. Zürich: ETH Zentrum, 1983. P. 257-262.

[21] Bergervoet, J.R. and G.P.J.F.M. Maas, M.J.C.M. van Doorn
The common-mode skeleton model for system-level EMC.
In: Proc. Electromagnetic compatibility 1997, 12th International Zurich symposium and technical exhibition on electromagnetic compatibility. Zürich, 18-20 February 1997. Zürich: ETH Zentrum, 1997. P. 657-662.

[22] Cloux, R. du and G.P.J.F.M. Maas, A.J.H. Wachters
Quasi-static boundary element method for electromagnetic simulation of PCBS.
Philips J. Res., Vol. 48 (1994), No's 1-2, p. 117-144.

[23] Horck, F.B.M. van and A.P.J. van Deursen, P.C.T. van der Laan
Coupling on a multilayer printed circuit board and the current distribution in the ground plane.
Eindhoven: Faculty of Electrical Engineering, Eindhoven University of Technology, 1996. EUT Report 96-E-300.

[24] Goedbloed, J.
Electromagnetic compatibility.
London: Prentice Hall, 1992.

[25] Ramo, S. and J.R. Whinnery, T. Van Duzer
Fields and waves in communication electronics. 3rd ed.
New York: Wiley, 1994.

[26] Balanis, C.A.
Antenna theory: Analysis and design. 2nd ed.
New York: Wiley, 1997.

[27] Taylor, C.D. and C.W. Harrison, Jr.
On the coupling of microwave radiation to wire structures.
IEEE Trans. Electromagn. Compat., Vol. EMC-34 (1992), No. 3, p. 183-188.

[28] Gupta, K.C. and R. Garg, I. Bahl, P. Bhartia
Microstrip lines and slotlines. 2nd ed.
Norwood, MA: Artech House, 1996.

[29] Bergervoet, J.R., private communication.

[30] Djordjević, A.R. and T.K. Sarkar, R.F. Harrington
Time-domain response of multiconductor transmission lines.
Proc. IEEE, Vol. 75 (1987), No. 6, p. 743-764.

[31] Djordjević, A.R. and T.K. Sarkar
Analysis of time response of lossy multiconductor transmission line networks.
IEEE Trans. Microwave Theory Tech., Vol. MTT-35 (1987), No. 10, p. 898-907.

[32] Smith, C.E. and R.-S. Chang
Microstrip transmission line with finite-width dielectric and ground plane.
IEEE Trans. Microwave Theory Tech., Vol. MTT-33 (1985), No. 9, p. 835-839.

[33] Pucel, R.A. and D.J. Massé, C.P. Hartwig
Losses in microstrip.
IEEE Trans. Microwave Theory Tech., Vol. MTT-16 (1968), No. 6, p. 342-350. Correction in IEEE Trans. Microwave Theory Tech., Vol. MTT-16 (1968), No. 12, p. 1064.

[34] Collin, R.E.
Foundations for microwave engineering, 2nd ed.
New York: McGraw-Hill, 1992.

[35] Djordjević, A.R. and T.K. Sarkar
Closed-form formulas for frequency-dependent resistance and inductance per unit length of microstrip and strip transmission lines.
IEEE Trans. Microwave Theory Tech., Vol. MTT-42 (1994), No. 2, p. 241-248.

[36] Faraji-Dana, R. and Y.L. Chow
Edge condition of the field and a.c. resistance of a rectangular strip conductor.
IEE Proc. H, Vol. 137 (1990), No. 2, p. 133-140.

[37] Faraji-Dana, R. and Y. L. Chow
The current distribution and ac resistance of a microstrip structure.
IEEE Trans. Microwave Theory Tech., Vol. MTT-38 (1990), No. 9, p. 1268-1277.

[38] Faraji-Dana, R. and Y. L. Chow
AC resistance of two coupled strip conductors.
IEE Proc. H, Vol. 138 (1991), No. 1, p. 37-45.

[39] Bladel, J. van
Electromagnetic fields. revised printing
Bristol: Hemisphere, 1985.

[40] Tijhuis, A.G. and P. Zhongqiu, A.R. Bretones
Transient excitation of a straight thin-wire segment: A new look at an old problem.
IEEE Trans. Antennas Propagat., Vol. AP-40 (1992), No. 10, p. 1132-1146.

[41] Weber, E.
Electromagnetic theory.
New York: Dover, 1965.

[42] Kuester, E.F. and D.C. Chang
Closed-form expressions for the current or charge distribution on parallel strips or microstrip.
IEEE Trans. Microwave Theory Tech., Vol. MTT-28 (1980), No. 3, p. 254-259.

[43] Coenen, M.
Optimising IC decoupling, for performance and EMI levels.
Electronic Prod. Des., Vol. 17 (1996), No. 1, p. 26, 29-30, 33-34.

[44] Djordjević, A.R. and T.K. Sarkar, R.F. Harrington
Analysis of lossy transmission lines with arbitrary nonlinear terminal networks.
IEEE Trans. Microwave Theory Tech., Vol. MTT-34 (1986), No. 6, p. 660-666.

[45] Paul, C.R.
Introduction to electromagnetic compatibility.
New York: Wiley, 1992.

[46] Collin, R.E.
Field theory of guided waves. 2nd ed.
New York: IEEE, 1991.

[47] Harrington, R.F. and K. Pontoppidan, P. Abrahamsen, N.C. Albertsen
Computation of laplacian potentials by an equivalent source method.
Proc. Inst. Electr. Eng., Vol. 116 (1969), No. 10, p. 1715-1720.

[48] Venkataraman, J. and S.M. Rao, A.R. Djordjević, T.K. Sarkar, Y. Naiheng
Analysis of arbitrarily oriented microstrip transmission lines in arbitrarily shaped dielectric media over a finite ground plane.
IEEE Trans. Microwave Theory Tech., Vol. MTT-33 (1985), No. 10, p. 952-959.

[49] Tikhonov, A.N. and A.A. Samarskii
Equations of mathematical physics.
New York: Dover, 1990.

[50] Harrington, R.F.
Field computation by moment methods.
New York: IEEE, 1993.

[51] Kaden, H.
Wirbelströme und Schirmung in der Nachrichtentechnik. 2nd ed.
Berlin: Springer, 1959.

[52] Gradshteyn, I.S. and I.M. Ryzhik
Table of integrals, series and products.
New York: Academic Press, 1967.

[53] Lewin, L.
Radiation from discontinuities in strip-line.
IEE Proc. C, Vol. 107 (1960), p. 163-170.

[54] Burke, G.J. and A.J. Poggio
Numerical electromagnetics code (NEC): Method of moments.
Lawrence Livermore National Laboratory, Livermore, California, 1981. Report 18834.

[55] Toit, C.F. du and D.B. Davidson
Wiregrid: A NEC2 pre-processor.
Appl. Comput. Electromagn. Soc. J., Vol. 10 (1995), No. 1, p. 31-39.

[56] Dettman, J.W.
Mathematical methods in physics and engineering.
New York: Dover, 1988.